



University of Bath  
Centre for Sustainable Chemical Technologies  
Department of Chemistry

# Computational Investigation of the Properties and Performance Bottlenecks of Selected Metal Sulfides for Use as Solar Absorber Materials

Suzanne K. Wallace

May 27, 2016



i



## Abstract

- Why metal sulfides - some have ideal optical properties and some are earth abundant?  
(look for book on sulfide minerals)
- Cu<sub>2</sub>ZnSnS<sub>4</sub> as a promising earth-abundant non-toxic solar absorber material for thin-film photovoltaic devices, theoretical conversion efficiency of 28% but major bottleneck of low open circuit voltage ( $V_{OC}$ ) relative to the band gap of the material.
- CZTS bottlenecks we address in this study
- Candidate photoferroelectric materials from screening process and properties for PV that we predict + novel properties of FE (Rashba splitting and FE domains for reduced recombination)

## Acknowledgements

I would like to express (whatever feelings I have) to:

- My supervisor
- My second supervisor
- Other researchers
- My family and friends

# Contents

<b>Abstract</b>	<b>ii</b>
<b>Acknowledgements</b>	<b>iii</b>
<b>1 Introduction</b>	<b>1</b>
1.1 The Case for New Solar Absorber Materials for Photovoltaic Devices . . . . .	1
1.1.1 Terawatt-Scale Power Production from Renewable Resources . . . . .	1
1.1.2 Basic Operating Principles of a Solar Cell Device . . . . .	5
1.1.3 Key Properties for Solar Absorber Materials . . . . .	9
1.1.4 Current Commercial Solar Cell Technologies & Limitations . . . . .	14
1.2 The Role of Computational Modelling in Material Design . . . . .	18
1.3 Overview of this Study . . . . .	19
1.3.1 Promising Candidate Solar Absorber Materials . . . . .	19
1.3.2 Investigating Possible Performance Bottlenecks of Cu <sub>2</sub> ZnSnS <sub>4</sub> Devices . .	23
1.3.3 Predicting the Properties of New Candidate Solar Absorber Materials . .	32

<b>2 Background Theory</b>	<b>39</b>
2.1 Models of Perfect Periodic Crystal Structures . . . . .	39
2.2 Band Theory & Band Structure of Semiconductors . . . . .	41
2.3 Crystal Imperfections & Disorder . . . . .	46
2.4 Solar Cell Performance Bottlenecks Due to Crystal Imperfections . . . . .	46
2.5 Characterization of Defects . . . . .	47
2.5.1 First-Principles Calculations . . . . .	47
2.5.2 Emission Spectroscopies of Semiconductors . . . . .	47
2.5.3 Photoluminescence Spectra of Cu <sub>2</sub> ZnSnS <sub>4</sub> . . . . .	48
2.5.4 Modulation Spectroscopy & Band Gap Broadening . . . . .	49
2.6 Novel Optoelectronic Phenomena for High Performance Solar Cells . . . . .	49
2.6.1 Spin Orbit Interaction & Rashba Splitting . . . . .	49
2.6.2 Photovoltaic-Ferroelectric Phenomena . . . . .	50
<b>3 Methodology</b>	<b>53</b>
3.1 Calculation of the Formation Energy of Defects in Cu <sub>2</sub> ZnSnS <sub>4</sub> . . . . .	53
3.1.1 Density Functional Theory & Hybrid Functionals . . . . .	54
3.1.2 The Supercell Method & Corrections for Charged Defects . . . . .	54
3.1.3 Defect Formation Energy & Equilibrium Concentration . . . . .	54
3.2 Monte Carlo Simulation of Thermodynamic Disorder in Cu <sub>2</sub> ZnSnS <sub>4</sub> . . . . .	54
3.2.1 Mapping the Crystal Structure of Cu <sub>2</sub> ZnSnS <sub>4</sub> onto a Simple Lattice . . .	54
3.2.2 Monte Carlo Simulation with the Metropolis Algorithm . . . . .	57

3.2.3	Equilibration & Finite Size Effects . . . . .	59
3.2.4	Multi-Scale Approach with Density Functional Theory . . . . .	62
3.2.5	Quantification of Disorder Using Radial Distribution Functions . . . . .	62
3.2.6	Band Tailing from the Distribution of Electrostatic Potential . . . . .	63
3.3	Calculation of Intrinsic Band Gap Broadening in Cu <sub>2</sub> ZnSnS <sub>4</sub> . . . . .	63
3.4	Calculation of Optoelectronic Properties of Candidate Solar Absorber Materials	63
<b>4</b>	<b>Performance Bottlenecks in Cu<sub>2</sub>ZnSnS<sub>4</sub></b>	<b>64</b>
4.1	Thermodynamic Disordering of Cu & Zn Ions in Cu <sub>2</sub> ZnSnS <sub>4</sub> . . . . .	64
4.1.1	Spatial Extent of Disorder Amongst Cu and Zn Cations . . . . .	64
4.1.2	Band Tailing due to Fluctuations in Electrostatic Potential . . . . .	64
4.2	Formation Energy of Sulfur Vacancies . . . . .	64
4.3	Intrinsic Band Gap Broadening from Lattice Vibrations . . . . .	65
<b>5</b>	<b>Optoelectronic Properties of Sulfosalt Materials</b>	<b>66</b>
5.1	Band Structures & Band Gaps . . . . .	66
5.2	Dielectric Functions . . . . .	66
5.3	Absorption Coefficients . . . . .	66
<b>6</b>	<b>Conclusions</b>	<b>67</b>
6.1	Performance Bottlenecks of Cu <sub>2</sub> ZnSnS <sub>4</sub> Solar Cells . . . . .	67
6.2	Potential of Sulfosalt Materials for Solar Cell Devices . . . . .	67
6.3	Future Work . . . . .	67





# List of Tables

1.1 Summary of known key properties of the three candidate photoferroelectric materials from the literature. . . . .	38
--	----



# List of Figures

1.1	Illustration of power available annually from various renewable energy resources, annual world energy consumption and total reserves of various non-renewable energy resources. Figure take from reference 133. . . . .	2
1.2	A building integrated photovoltaics (BIPV) project fitted in the United States by BISEM-USA [11]. . . . .	3
1.3	Levelized cost of electricity (LCOE) of renewable energy technologies and conventional power plants at locations in Germany in 2013. Specific investments are taken into account with a minimum and maximum value for each technology. Figure taken from reference 38. . . . .	4
1.4	Schematic of a typical crystalline silicon solar cell device (top), where the majority of the cell consists of a thick p-type base in which most of the light is absorbed. After light absorption, the minority carriers (electrons) diffuse to the junction where they are swept across by the strong built-in electric field. The electrical power is collected by metal contacts to the front and back of the cell. Excitation of an electron-hole pair across the band gap of the p-type material (bottom). Figure taken from reference 84. . . . .	6
1.5	The current-voltage (I-V) curve of a solar cell showing the open circuit voltage ( $V_{OC}$ ). Figure taken from reference 56. . . . .	7

1.6 AM1.5 solar spectrum with distinct dips due to molecular absorption in Earths atmosphere. The dashed line shows the band gap of silicon and fading to the left indicates that photons with energies below the band gap will not be absorbed and other fading indicates other loss mechanisms that prevent a solar cell from being unable to convert the full incident spectrum into electricity. Figure taken from reference 104.	9
1.7 Theoretical Shockley-Queisser detailed-balance efficiency limit as a function of band gap[119] (highest black line). The record efficiencies for different materials are plotted for the corresponding band gaps, where materials below the lower two grey lines are achieving conversion efficiencies less than 75% and 50% of their theoretical efficiency limit respectively. Figure taken from reference 104.	10
1.8 Polarization mechanisms in a crystalline solid: response of electronic density and motion of ions (a), figure taken from 92. Typical frequencies of applied electric field to induce polarization mechanisms, where the response at high frequencies is only that of the electronic density (b), figure adapted from reference 57.	12
1.9 Average cost of solar panels composed of a crystalline silicon absorber layer. Figure taken from reference 118.	15
1.10 Efficiency and cost projections for first-, second- and third-generation photovoltaic technologies, which are comprised of silicon wafer, thin-film and advanced thin-film technology respectively. Figure taken from reference 44.	16
1.11 The conventional unit cell of CZTS ( $\text{Cu}_2\text{ZnSnS}_4$ ) with the ground-state kesterite crystal structure (space group $I\bar{4}$ ). The structure consists of alternating layers of Cu-Sn and Cu-Zn where Cu-Zn layers are at $z=\frac{1}{4}$ and $z=\frac{3}{4}$ .	23
1.12 Mapping of the numerous possible mechanisms limiting the efficiency in kesterite devices and their possible causes. $R_s$ is the series resistance between the absorber layer and back contact of the device and $V_{OC}$ is the open circuit voltage across the absorber layer. Figure take from 30.	24

1.13 $V_{OC}$ versus band gap of high performance CZTSSe devices (>9% efficiency) indicated by circles with best devices based on other photovoltaic materials shown for comparison by diamond symbols: Methyl-ammonium lead iodide (MAPI), amorphous silicon (a-Si), organic photovoltaic films (OPV), crystalline silicon (c-Si) and polycrystalline silicon (pc-Si). The oblique lines give a constant $V_{OC}$ deficit from 0.8 V to 0 V. The green points correspond to CZTSSe films that are partially ordered (PO) or partially disordered (PD) due to disorder amongst Cu and Zn. Figure take from reference 17. . . . .	25
1.14 Internal quantum efficiency (IQE) and photoluminescence (PL) spectra of CZTSSe thin-films showing the shift of the PL peak to energies below the band gap of the material. Figure take from reference 47. . . . .	26
1.15 Illustration of Shockley-Read-Hall (SRH) electron-hole recombination due to energy states introduced into the band gap by defects. . . . .	27
1.16 The effect of electrostatic potential fluctuations (a) and band gap fluctuations (b) on the electronic bands of a semiconductor. In both cases radiative transitions at energies below the (average) band gap are possible. The band gap in a is constant and not affected by local charged defects, while band edges in b can differ depending on e.g., long range composition variations. Figure taken from reference 17. . . . .	28
1.17 The formation energy of neutral intrinsic defects in $\text{Cu}_2\text{ZnSnS}_4$ as a function of the chemical potential. Figure taken from reference 27. . . . .	30
1.18 The transition-energy levels of intrinsic defects in the band gap of $\text{Cu}_2\text{ZnSnS}_4$ where the GGA band gap has been corrected to the experimental value 1.5 eV, and the donor levels are shifted together with the conduction band minimum (CBM) level. Figure taken from reference 27. . . . .	31
1.19 The formation energy of charge compensated defect complexes in $\text{Cu}_2\text{ZnSnS}_4$ as a function of the chemical potential. Figure taken from reference 27. . . . .	32

1.20 The conduction band minimum (CBM) and valence band maximum (VBM) levels in eV of Cu <sub>2</sub> ZnSnS <sub>4</sub> with different charge-compensated defect complexes relative to the host material at 0 eV and 1.5 eV respectively. Figure taken from reference 27.	33
1.21 Venn diagram showing the necessary (but not sufficient) conditions for a material to exhibit photoferroelectricity, where the dark colour suggests absorption of light in the visible range and a polar crystal structure is a requirement (but does not serve as a guarantee) for a material to exhibit ferroelectricity.	34
1.22 Comparison of element abundance and price between Cu, In, Ga, Cd, Sb, Sn, S, Se and Te. Figure taken from the supporting information of reference 144, where data was taken from the London Metal Exchange LME.	35
1.23 The 15 atom primitive unit cell of enargite (Cu <sub>3</sub> AsS <sub>4</sub> ) (a), 19 atom primitive unit cell of stephanite (Ag <sub>5</sub> SbS <sub>4</sub> ) (b) and 23 atom primitive unit cell of bournonite (PbCuSbS <sub>3</sub> ) (c).	36
2.1 The Wigner-Seitz cell for the body-centred cubic Bravais lattice where there is a lattice point at its centre and on each vertex. The hexagonal faces bisect the lines joining the central point to the points on the vertices. The square faces bisect the lines joining the central point to the central points in each of the six neighbouring cubic cells. Figure taken from reference 2.	40
2.2 Electron energy levels of a single atom (left) and the formation of a quasi-continuous band of allowed energies in a solid crystal when many atoms are brought close together (right). Figure taken from 102.	42
2.3 Energy-wave vector diagrams: (a) the free electron parabola, (b) modification due to a periodic crystal lattice. Figure taken from reference 70.	43

2.4	The energy dispersion relation for electrons moving in a crystal, illustrating how the function can be approximately represented by a finite number of $k$ -points, which form an equally-spaced mesh. Figure adapted from reference 36. . . . .	44
2.5	The influence of increased donor impurity density on the conduction band profile showing low (a), medium (b) and high (c) densities of impurities. Figure taken from reference 71. . . . .	45
3.1	A supercell of the perfect $\text{Cu}_2\text{ZnSnS}_4$ crystal lattice, which can be described by inter-penetrating face-centred cubic sub-lattices: one of metal cations and one of sulfur anions. Green planes are used as guides to the eye to show planes of S anions that form one of the two face-centred cubic sub-lattices. . . . .	55
3.2	A two-dimensional (x-y) slice of a 20x20x20 cation sub-lattice of ordered $\text{Cu}_2\text{ZnSnS}_4$ . Sulfur anions are neglected from the simulations and the face-centred cubic cation lattice is mapped onto a simple cubic lattice by including empty sites in the lattice. Alternating layers in the z-direction are displaced by one lattice unit in order to reproduce the correct kesterite structure. ‘C’, ‘Z’, ‘T’ and ‘.’ represent copper, zinc, tin and an empty site respectively. . . . .	56
3.3	Flat visuals of the $\text{Cu}_2\text{ZnSnS}_4$ crystal structure showing positions of empty sites (denoted by x’s) used to map the face-centred cubic lattice of the cations onto a simple cubic lattice. Lattice parameters obtained from hybrid density functional theory geometry optimizations are $a = b = 5.43770 \text{ \AA}$ and $c = 10.85670 \text{ \AA}$ , and so $c$ is approximately $2a$ . . . . .	56
3.4	The magnetization (upper curve) and internal energy (lower curve) per site of a two-dimensional Ising model simulated using the Metropolis algorithm (a). Magnetization as a function of time for two different simulations (b). Time is measured in Monte Carlo steps per lattice site. Figures taken from 91. . . . .	60
3.5	Typical periodic boundary conditions for the two-dimensional Ising model. Figure taken from 75. . . . .	61



# Chapter 1

## Introduction

### 1.1 The Case for New Solar Absorber Materials for Photovoltaic Devices

#### 1.1.1 Terawatt-Scale Power Production from Renewable Resources

It is now widely accepted that the world is heading towards a major energy crisis, where there will come a point that the current major sources of energy (namely fossil fuels) will be unable to meet increasing global demand for energy as they are not a limitless supply. Furthermore, there is the ever present worry of climate change linked to increased carbon dioxide emissions from the burning of fossil fuels. Renewable, low-carbon alternative energy sources are therefore clearly desirable. From purely environmental considerations, it seems clear that fossil fuels should no longer be used and we should meet our energy needs solely from renewable, low-carbon energy resources such as solar power. However, it is not only environmental sustainability that must be considered, we must also consider the economic feasibility of solar power for large-scale projects. Germany is an example of a country making considerable efforts to increase the percentage of their energy supplied by solar power. On 9 June 2014 Germany even generated over 50% of its electricity demand from solar for the first time [137]. Although on average the country is not able to produce such a large portion from solar power, with solar-generated power providing

approximately 7.5% of net electricity consumption in 2015 [140]. To facilitate the growth of the solar power capacity in Germany a number of schemes and financial incentives to encourage investment were introduced, such as feed-in tariffs (FiTs). The German government first introduced FiTs in their Grid Feed-In Law (the Stromeinspeisegesetz), which came into force in 1991 [77]. FiTs are intended to support new developments in renewable energy supply by providing investor certainty. They set the rate a utility company must pay for renewable generated energy and guarantee the provider of renewable energy a specific rate for a long period of time, typically fifteen to twenty years. As this cost is higher than fossil fuel based electricity, the higher price is then passed on to all customers of the utility company to spread out the higher costs so that buyers of renewable energy do not pay higher prices. In Germany, this has resulted in an increase of 6% on the average electricity bill for users in a specific region [94]. The social implications of such a cost increase must also be considered in assessing the viability of a particular power source.

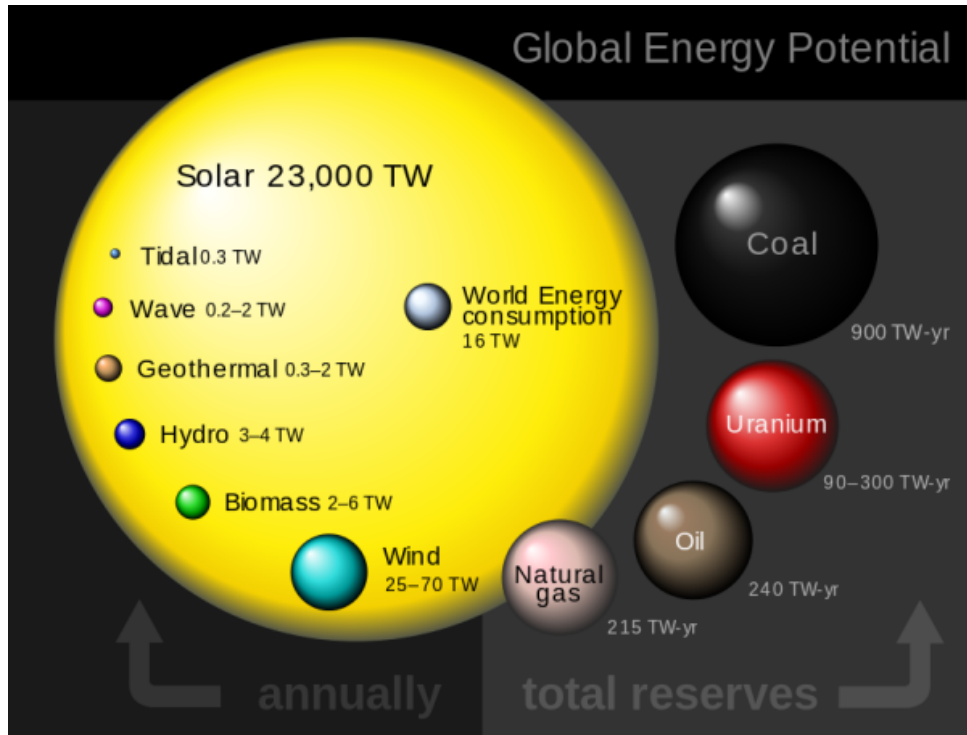


Figure 1.1: Illustration of power available annually from various renewable energy resources, annual world energy consumption and total reserves of various non-renewable energy resources. Figure take from reference 133.

However if solar power, in combination with proper energy transport, storage and secondary

conversion into heat and fuels, could be made to be economically feasible; it is a realistic candidate for replacing fossil fuels as a major supply of global energy. It is by far the largest source of energy available to us, as illustrated in figure 1.1, and it is also the most widely geographically distributed [62]. The Sun supplies  $3 \times 10^{24}$  J of energy to the Earth each year, which is around  $10^4$  times more than mankind's current annual energy consumption. Assuming a fairly modest module efficiency of 20%, a system capacity factor of 15%, an average ground cover ratio of 50%, and 50% losses related to storage and secondary conversion, 1.6% of the Earth's land area would be required for solar-generated power to meet current world energy needs [104]. Although this would be a fairly large area, it would not be completely unrealistic. For instance, this area would be less than 5% of the area used for agriculture worldwide [104]. The area required could also be reduced further through improvements in the efficiency of PV module and by making use of building-integrated PV (BIPV) innovations, largely made possible by flexible, thin-film second generation PV technologies which are discussed further in section 1.1.4. An example of a BIPV project is shown in figure 1.2, where solar panels are not only placed on the roof of a building but can also placed on the windows and outer walls.



Figure 1.2: A building integrated photovoltaics (BIPV) project fitted in the United States by BISEM-USA [11].

Recent years have seen a rapid increase in the installed solar generation capacity, with the

global grid-connected PV capacity growing from 1.3 GW in 2000 to 139 GW in 2014 [4], with approximately a doubling in the cumulative installed capacity every two years [66]. Additionally, creative business models have spurred investment in residential solar systems [95]. Great improvements in technology, price and performance have helped to facilitate this growth, but solar energy still only provides a minor fraction of the world's energy. In 2013 solar power only provided 0.87% of the world's electricity [106]. Further advances are required to enable a dramatic increase in the contribution from solar power at socially acceptable costs [95]. Ultimately, solar power-generation technologies must become cost-competitive with conventional fossil-fuel based power sources.

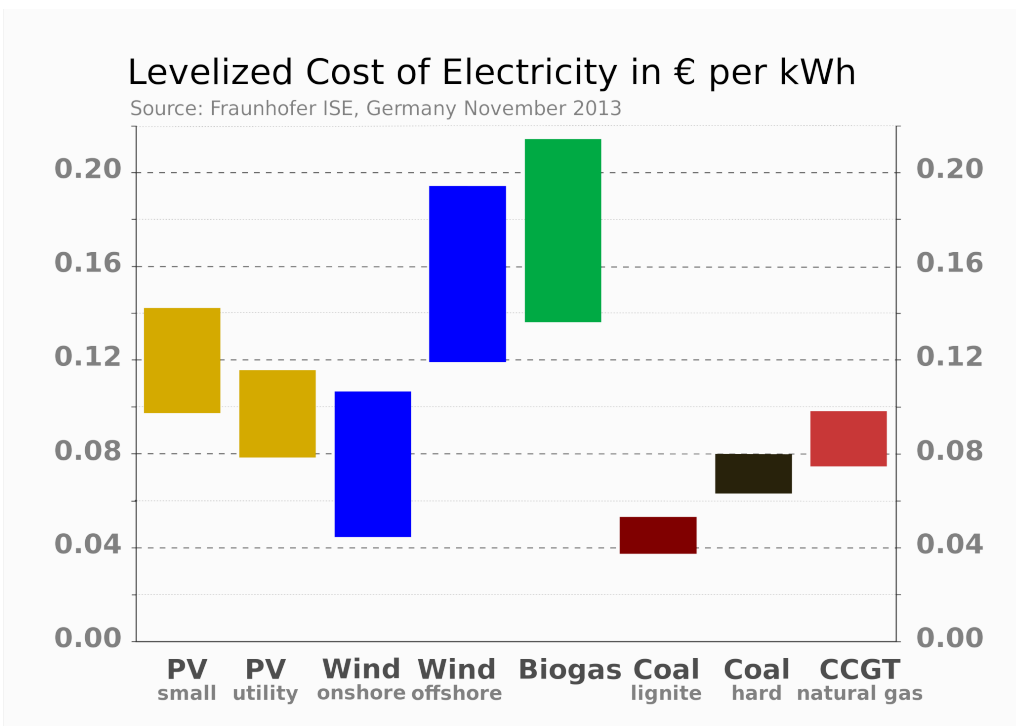


Figure 1.3: Levelized cost of electricity (LCOE) of renewable energy technologies and conventional power plants at locations in Germany in 2013. Specific investments are taken into account with a minimum and maximum value for each technology. Figure taken from reference 38.

Levelized cost of energy, or electricity, (LCOE) is a common way to assess how cost competitive renewable energy sources are with their non-renewable counterparts. LCOE allows for the measurement of the performance of different power generating technologies, which may have unequal lifetimes and differing capacities. It is calculated by summing all costs incurred during

the lifetime of the technology and dividing this value by the units of energy produced during the lifetime, with units of energy expressed as dollars per kilowatt hour (\$/kWhr) [82]. This measure is also used as the key selling point for a number of commercial solar cell manufacturers such as First Solar Inc., who market their product as being able to generate electricity at an average of \$0.63 per Watt as stated in their 2013 Annual Report [61]. Using the LCOE, comparisons of grid competitiveness for renewable energy sources can be made [82]. Figure 1.3 shows the LCOE of renewable energy technologies and conventional power plants at locations in Germany in 2013, enabling an assessment of the cost-competitiveness of PV power generation at this location, accounting for, for example, typical solar irradiation at the given locations [38]. As the figure shows, both small-scale and large-scale utility solar power are still not cost competitive with the cheapest non-renewable resources.

### 1.1.2 Basic Operating Principles of a Solar Cell Device

Refer to: pg 5 [15], pg 11 + 18 [46]

A solar cell device converts solar energy directly into electrical energy, where solar energy can be described as either a spectrum of electromagnetic radiation or a flux of photons ???(and electrical energy is a flow of charge carriers able to do work in an external circuit.)??? [15] Voltage is generated in a solar cell device by the photovoltaic effect. The terms ‘solar cell’ and ‘photovoltaic (PV) cell’ are therefore often used interchangeably.

Semiconducting materials are usually utilized in a PV device. A semiconductor is described by its valence and conduction energy bands i.e. a group of energy levels, which electrons may occupy, and a gap in between with no available energy levels called the bandgap. In thermal equilibrium at a 0 K, all the energy levels in the valence band are occupied by electrons while all energy levels in the conduction band remain unoccupied. Energy level occupancy at temperais usually described by the Fermi-Dirac distribution [1]. [15]

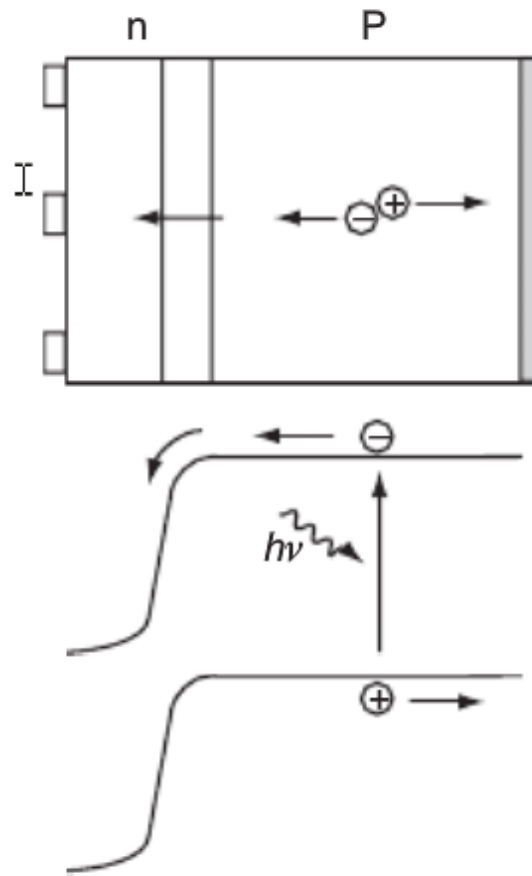


Figure 1.4: Schematic of a typical crystalline silicon solar cell device (top), where the majority of the cell consists of a thick p-type base in which most of the light is absorbed. After light absorption, the minority carriers (electrons) diffuse to the junction where they are swept across by the strong built-in electric field. The electrical power is collected by metal contacts to the front and back of the cell. Excitation of an electron-hole pair across the band gap of the p-type material (bottom). Figure taken from reference 84.

Only photons with energies higher than the bandgap can be absorbed in the perfectly pure semiconductor by exciting an electron from the valence to the conduction band, while simultaneously conserving total energy and momentum. Two types of semiconductors are distinguished with regards to the shape of the valence and conduction band in the energymomentum diagram. In a direct semiconductor, the maximum energy of the valence band and the minimum energy of the conductance band are located at the same momentum, which is not the case in an indirect semiconductor. Light absorption in a direct semiconductor occurs when the photon interacts with only an electron from the valence band. Light absorption in an indirect semiconductor requires a phonon (i.e. a quantum of thermal energy with considerable momentum, which is discernible as a crystal lattice vibration) assisted transition, where a phonon provides

or consumes the difference in momentum. [15]

When semiconducting materials absorb photons of light with energies of at least their band gap, electrons are excited to higher energy states within the material to form an electron-hole pair, as shown in figure 1.4. The excited electron-hole pair would eventually recombine and relax back to the ground state of the material with the emission of a photon of an energy equal to the energy of the electronic transition that has just occurred. However in a PV device, there is a built-in asymmetry that leads excited charge-carriers away before they can recombine back to the ground state. The extra energy of the excited electron generates a potential difference that drives electrons through a load in the external circuit to do electrical work. In the conventional PV effect, as electrons are excited across the band gap of a semiconductor, the band gap of the material sets the upper limit for the maximum voltage that can be generated. In early PV devices, the asymmetric junction was a Schottky barrier between a metal and a semiconductor but now more effective p-n junctions are used, which are formed by joining together p-type and n-type semiconductors [89].

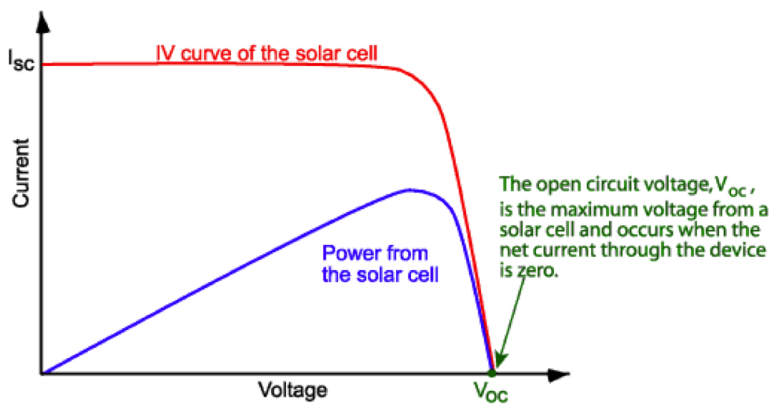


Figure 1.5: The current-voltage (I-V) curve of a solar cell showing the open circuit voltage ( $V_{OC}$ ). Figure taken from reference 56.

When a cell consisting of a p-n junction is illuminated, a voltage develops across the terminals, i.e. between the p-type and n-type semiconductors. When the terminals of the solar cell are disconnected from any external circuit, or there is an infinite load resistance, this voltage is at a maximum and is called the open circuit voltage ( $V_{OC}$ ) and no current is drawn from the solar cell. Conversely, if the terminals of the solar cell are connected together then there is

no voltage as all of the electromotive force is used to extract charge-carriers. The maximum possible current is drawn, which is called the short circuit current ( $I_{SC}$ ). For a solar cell to generate power, there must be both voltage and current generated, therefore when the cell is operating at either  $V_{OC}$  or  $I_{SC}$  the power output is zero. To generate power, a finite load resistance is added to the circuit so that some current is drawn from the solar cell and a voltage develops across the cell that is between 0 and  $V_{OC}$  [89]. There is a maximum operation point for the power output ( $P_{MP}$ ) of a solar cell in terms of I and V, as shown in figure 1.5. This can be defined in terms of  $V_{OC}$  and  $I_{SC}$  when used in conjunction with the fill factor (FF), which is a number less than one that describes the squareness of the I-V curve [50] shown in figure 1.5 and is given by equation 1.1. The current and voltage are determined by the load and illumination so the load can be tuned such that maximum power output is achieved, but the value of  $V_{OC}$  places a limit on the power output of the cell [89].

$$P_{MP} = FFV_{OC}I_{SC} \quad (1.1)$$

$$\eta = \frac{P_{MP}}{P_{in}} = \frac{FFV_{OC}I_{SC}}{P_{in}} \quad (1.2)$$

The power conversion efficiency (PCE),  $\eta$ , of a solar cell is the ratio of power output from the solar cell to the power input from the Sun. This is shown in equation 1.2, where  $P_{MP}$  has been taken from equation 1.1. For an efficient solar cell, it is desirable to have a high  $I_{SC}$ , a high  $V_{OC}$  and a FF that is as close to 1 as possible [50].

\*\*Move discussion to section on candidate new materials\*\* CZTS solar cells are known to be hampered by low  $V_{OC}$  relative to the band gap of the material [122]. Whereas in ferroelectric PV materials, photovoltages orders of magnitude larger than the band gap have been measured (a phenomena referred to as the anomalous photovoltaic effect), but very low photocurrent output is a big challenge for these devices [150].

\*\*Add figure and description of basic PV device + show basic simplified band diagram (later compare to real band structure, e.g. of Si)\*\*

A solar cell device consists of... (see Mirjana's thesis)

### 1.1.3 Key Properties for Solar Absorber Materials

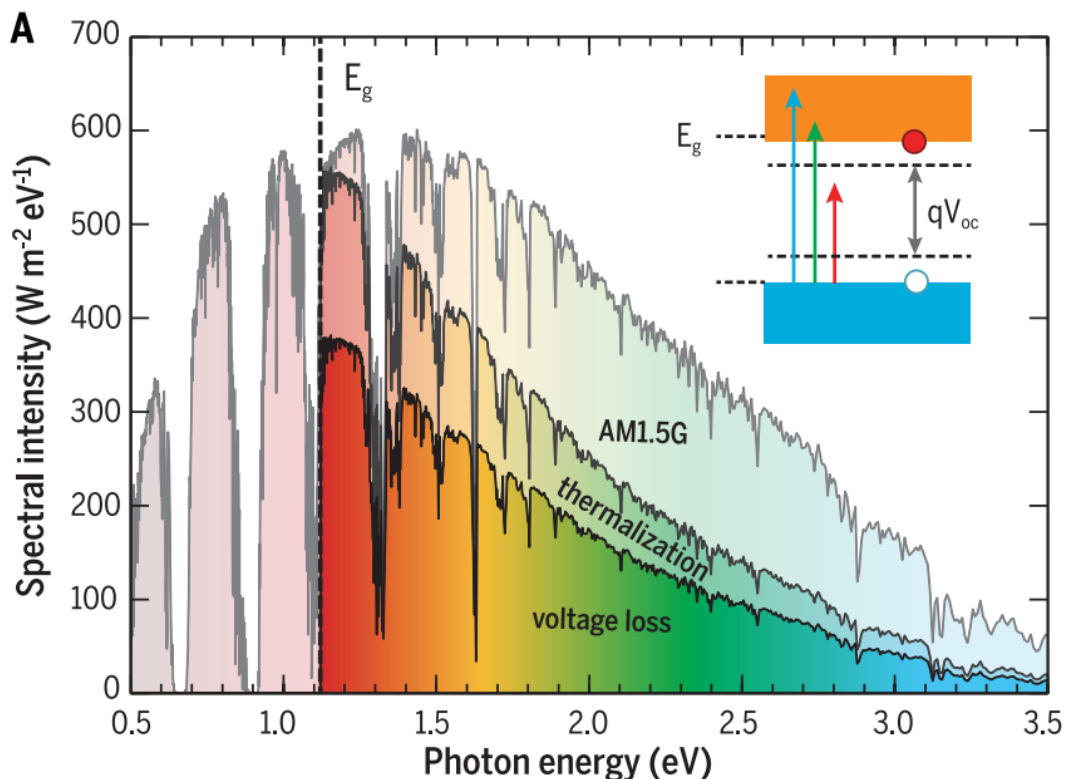


Figure 1.6: AM1.5 solar spectrum with distinct dips due to molecular absorption in Earth's atmosphere. The dashed line shows the band gap of silicon and fading to the left indicates that photons with energies below the band gap will not be absorbed and other fading indicates other loss mechanisms that prevent a solar cell from being unable to convert the full incident spectrum into electricity. Figure taken from reference 104.

A solar (or photovoltaic) cell is an example of an optoelectronic device in which the solar absorber material of choice must allow for the manipulation of light, electrical current and their interaction. Metals are excellent electrical conductors, but do not allow light to travel inside. Glass and related dielectric materials can accommodate and guide light waves, as in electrical fibres, but are electrical insulators. Semiconductors are in between these two types

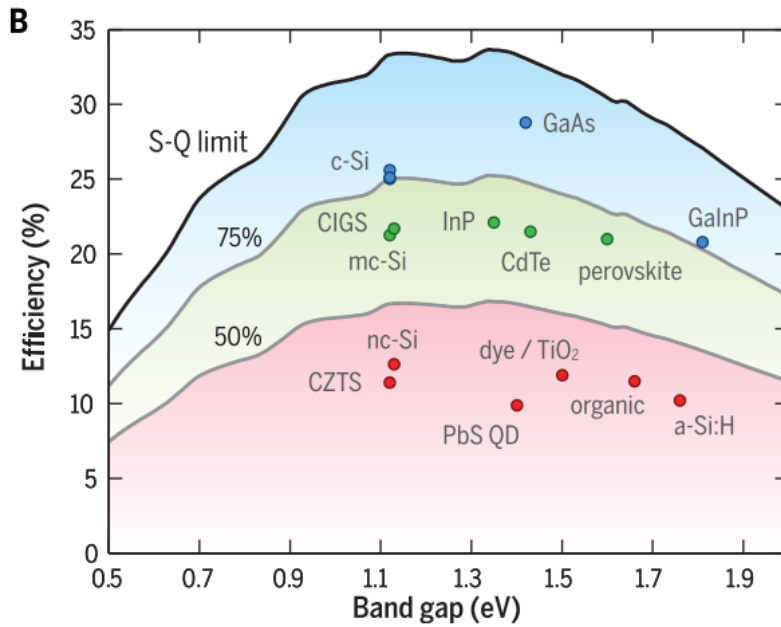


Figure 1.7: Theoretical Shockley-Queisser detailed-balance efficiency limit as a function of band gap[119] (highest black line). The record efficiencies for different materials are plotted for the corresponding band gaps, where materials below the lower two grey lines are achieving conversion efficiencies less than 75% and 50% of their theoretical efficiency limit respectively. Figure taken from reference 104.

of material as they can carry both electrical current as well as light waves. Furthermore, some semiconductors can be used to transform light into electrical current as discussed in the section above [102]. The two vital processes that must occur in a solar absorber material were also discussed above, which were: the excitation of an electron from the valence band into the conduction band in a semiconducting material by a photon and subsequent collection of the photoexcited charge carriers by an external circuit before the photoexcited electron-hole pair recombine. There are certain optical and electrical properties that are necessary for these processes to occur and then there are also certain properties that indicate how well a material is likely to perform in a solar cell device. In this section the band gap, effective mass, dielectric constant and absorption coefficient of a potential solar absorber material will be discussed.

The most obvious necessary requirement for a solar absorber material is for it to be a semiconductor so that it possesses a band gap across which an electron can be excited. The value of this band gap must also be somewhere within the solar spectrum shown in figure 1.6 so that sunlight can induce the photoexcitation of an electron-hole pair across the band gap. Secondly

the material must allow for transport of charge carriers out of the absorber material and into a collection electrode and external circuit. Provided these necessary conditions are met and some sort of bias is applied to drive the separation of the electron-hole pair, the material should exhibit the photovoltaic effect. However, how well it will actually perform in a solar cell is determined by more stringent criteria and other material properties. Firstly the actual value of the band gap within the range of the solar spectrum is of importance. It is ideal for the value to be as close as possible to the region of photon energies that make up the majority of the solar spectrum. The optimal range for the band gap under typical radiation conditions is between 1.06 eV and 1.50 eV [63]. The limit of the power conversion efficiency (of incident photon energy to electrical energy) of a material based on its band gap was first calculated with Shockley and Quieser in 1961 [119] and a plot of theoretical efficiency limit as a function of band gap is shown in figure 1.7.

However, it is not only the value of the band gap that is of importance, whether the gap is direct or indirect is also of importance... e.g. of Si vs GaAs + calc from lectures

Another property of importance that can be derived from the band structure of a material is the effective mass... The effective mass is related to the curvature of the band at the top of the valence band or at the bottom of the conduction band Effective mass + band curvature and carrier collection? (refer to figs from section above) - can give some info on carrier mobility Effective mass and electrical conductivity discussion. Although certain thin-film technologies discussed towards the end of section 1.1.4 reduce the amount of absorber material the charge carrier must travel through before being collected. The effective masses of electrons or holes are the masses they seem to carry for transport properties.

Materials with ionic or covalent bonding, or a mixture of the two, are usually either insulators or intrinsic semiconductors. Due to this type of bonding, electrons are bound to the atomic structure and so are unable to move throughout the material when an electric field is applied as in a metal. However, these materials can be polarized by an applied electric field where electrons are displaced relative to their nuclei by small distances. When an external electric

field is applied, the positive and negative charges experience electric forces tending to move them apart in the direction of the external field so that their centres of gravity no longer coincide [152]. The material is now said to be polarized and an electric displacement field ( $\vec{D}$ ) appears within it. The applied field ( $\vec{E}$ ) and displacement field are linked by the dielectric constant of the material,  $\epsilon_r$ , as shown by equation 1.3 [5].

$$\vec{D} = \epsilon_0 \epsilon_r \vec{E} \quad (1.3)$$

The dielectric constant indicates the ability of a material to screen the external electric field by the apparition of a polarization. In a solid, this polarization comes from the re-organization of the electronic density or from the motion the ions that make up the material. These two mechanisms are illustrated in figure 1.8a and associated frequencies of the applied field to induce particular polarization responses are shown in figure 1.8b. The contribution to the dielectric constant from the electronic density is denoted as  $\epsilon_\infty$  and the contribution of ionic motions is denoted  $\epsilon_{vib}$  in equation 1.4 [5].

$$\epsilon_r = \epsilon_\infty + \epsilon_{vib} \quad (1.4)$$

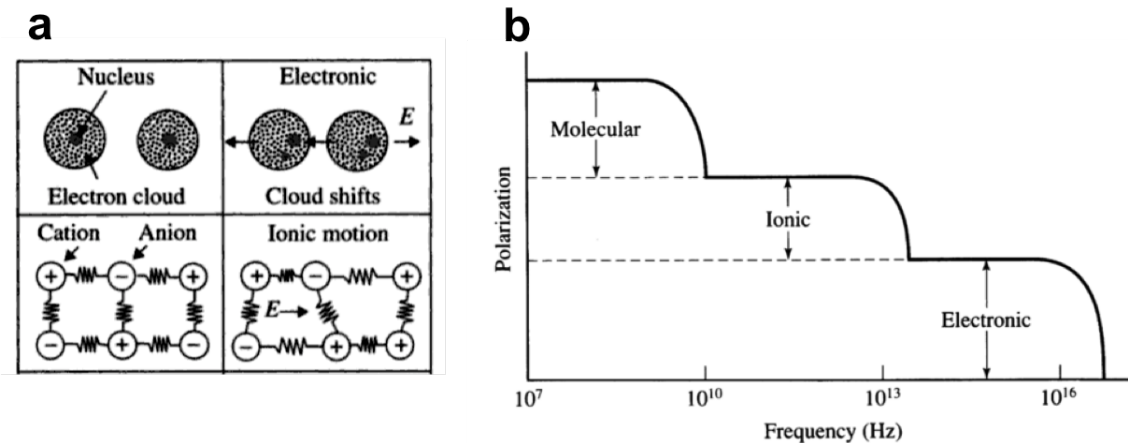


Figure 1.8: Polarization mechanisms in a crystalline solid: response of electronic density and motion of ions (a), figure taken from 92. Typical frequencies of applied electric field to induce polarization mechanisms, where the response at high frequencies is only that of the electronic density (b), figure adapted from reference 57.

The dielectric constant is an important material property for a photovoltaic material for a number of reasons. Firstly, the electrostatic force between an electron-hole pair is reduced when

$\epsilon_r$  is larger [5]. This, therefore, will reduce the recombination of electron-hole pairs in a material. Another aspect of this property important for photovoltaic materials is that it can improve the defect tolerance of the material, as in the majority of cases producing perfectly defect-free materials is impractical, if not impossible. The impact of defects in a material on photovoltaic performance will be discussed more in section 2.4, but for now it is just worth noting that defects can trap charge carriers, enhance electron-hole recombination (reducing carrier lifetimes in the material) and therefore have the overall effect of reducing charge collection from a PV device, thereby decreasing the efficiency of the conversion of incident photons into electrical current. In reference to modelling electronic transport in a material in the presence of defects,  $\epsilon_r$  has been referred to as the most important property of the material [18]. A higher dielectric constant indicates a greater ability to screen charge. The capture cross-section for charge carriers by a charged defect will therefore be influenced by the value of  $\epsilon_r$  of the material [18]. This property can therefore indicate how well photo-excited charge carriers will be transported through a defective photovoltaic material, towards an electrode for carrier collection and on to do electrical work.

The dielectric constant of a material is also important when considering how strong the onset of absorption is.

The band gap determines which photons can be absorbed by a material, but it does not predict how strongly that material will absorb them. As solar absorber materials can only absorb photons with energies larger than the band gap of the material, these materials typically have an abrupt edge in its absorption coefficient, however the onset of absorption can be more or less strong for different materials. The absorption coefficient depends on both the particular material and the energy of the light being absorbed.

SLME + absorption coeff + dielectric const?

### 1.1.4 Current Commercial Solar Cell Technologies & Limitations

It was first observed in 1839 by Edmond Becquerel that sunlight could be used to generate electricity. Becquerel discovered that if silver chloride was placed in an acidic solution, connected to platinum electrodes and exposed to sunlight, an electric current flowed. However the effect was small and poorly understood before Albert Einstein's discovery of the photoelectric effect and explanation of the phenomena by the quantum nature of light in 1904 [124]. Even then, it was not until the development of semiconductor technology during the silicon revolution of the 1950's that solar cells were fabricated which were able to generate significant amounts of electricity. The first silicon solar cell was created in 1954 in the Bell Laboratories with cells achieving efficiencies of 6%. Originally solar cells were developed for terrestrial energy generation, such as the 108 solar cells used to supply energy to the Vanguard satellite in 1958 [124]. The first oil crisis in 1973 however highlighted the dependency of many economies on fossil fuels and the need to address the security of energy supply, in particular for Japan and West Germany which had few of their own resources. As a consequence, solar cell research was no longer limited to only high-cost crystalline silicon devices for terrestrial applications, but also into creating cheaper, commercial, thin-film solar cell technologies using absorber materials such as amorphous silicon, cadmium telluride and copper indium diselenide [76].

In spite of this, crystalline silicon is still the dominant solar cell technology with mono- and poly-crystalline silicon photovoltaic cells comprising up to 90% of all the solar cells produced in 2008 [110]. Silicon is the second most abundant element in the Earth's crust [45], making it a plausible material to use in large-scale solar power generation. Over 60 years of development have seen device efficiencies increase from 6% to 25% for the highest quality research devices and 15-18% for the more common industrial cells [110]. As can be seen from figure 1.7, the best performing silicon devices are now very close to achieving conversion efficiencies close to their theoretical limit, as predicted by Shockley-Quiesser [119]. More dramatic however is the fall in manufacturing costs which have halved since 2008 and are more than a hundred times lower than they were in 1977, as shown in figure 1.9. This development was largely aided by

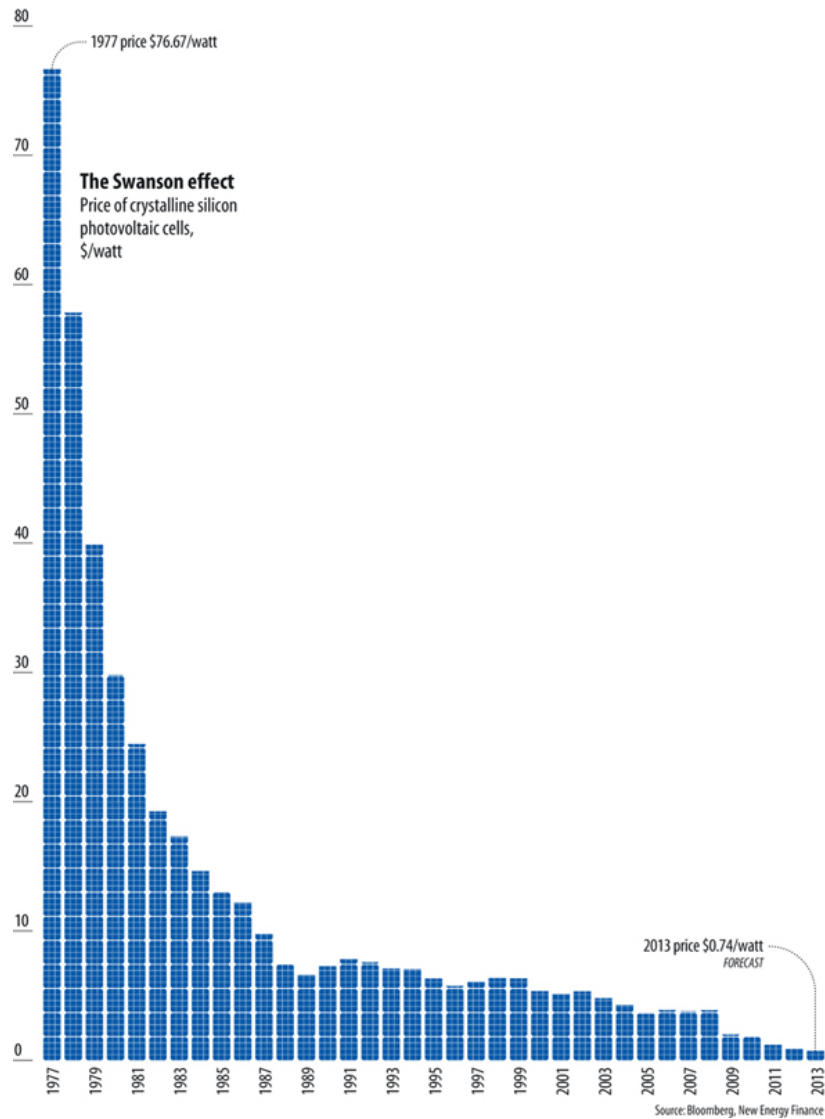


Figure 1.9: Average cost of solar panels composed of a crystalline silicon absorber layer. Figure taken from reference 118.

progress in semiconductor technology driven by the silicon chip industry, with the solar industry benefiting from advances in silicon manufacturing processes and even making use of waste silicon produced that was not of a high enough grade for silicon chips [124]. Although the development of silicon-based technologies has clearly revolutionized the modern computer, the optical properties of silicon do not make it ideal for use as a solar absorber material in a photovoltaic device and despite the dramatic reduction in manufacturing costs, the technology is still not able to be cost-competitive with fossil-fuel power generation, as was shown in figure 1.3.

The primary issue with silicon is that its band gap of 1.1 eV is indirect. The key consequence

of this property is that silicon is therefore not a very strong absorber of sunlight (compared to for instance newer, thin-film technologies which are discussed later), resulting in a low optical absorption coefficient compared to these newer technologies where both band gap and absorption coefficient were two of the key material properties for solar cells discussed in section 1.1.3. To absorb the same amount of sunlight with a silicon solar cell requires a thicker layer of the material than in thin-film technologies. Photovoltaic devices are very sensitive to defects and impurities. This point is discussed further in section 2.4, but the consequence for a thick layer of silicon is that very high quality, non-defective material is necessary to enable charge carrier collection before recombination occurs, which results in high manufacturing costs. The devices are made from flat sheets of crystalline or multicrystalline silicon called wafers that consist of very high quality silicon (99.99999% pure) [93]. The production processes of silicon wafers have been thoroughly optimised, but are still very energy-intensive, time-consuming and complex [53] and this is reflected by the position of this type of technology on the plot of efficiency versus cost shown in figure 1.10. Despite decades of development, commercialized silicon solar panels are still too expensive to compete with fossil-fuel based power sources [117].

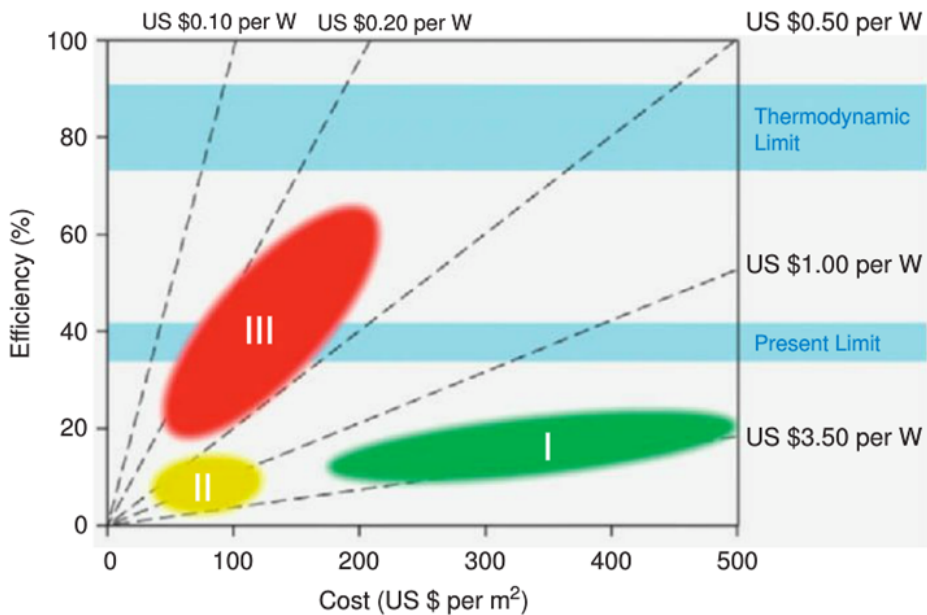


Figure 1.10: Efficiency and cost projections for first-, second- and third-generation photovoltaic technologies, which are comprised of silicon wafer, thin-film and advanced thin-film technology respectively. Figure taken from reference 44.

The ‘holy grail’ of research into new materials for photovoltaic devices would be to find materials that are strong absorbers of sunlight that could also be produced cost-effectively from materials that are abundant enough for large-scale fabrication of the devices. Then it could be possible for solar energy generation to be economically viable on a large enough scale to replace fossil fuels to meet global energy needs. Such a drive has resulted in the development of what are considered three generations of solar energy technology. These are shown in figure 1.10, where highly efficient crystalline silicon devices with high associated manufacturing costs are considered the first generation of solar cell technology. Thin-film solar cell devices are typically referred to as second-generation technology. These devices make use of materials that are much more optically thick than silicon (i.e. stronger absorbers of sunlight with higher optical absorption coefficients), which require less material to absorb the same amount of sunlight. It is then less important for the material to be of as high-quality as in crystalline silicon devices, which enables the use of low-cost and low-energy fabrication methods [53]. In the case of thin-film CuInSe<sub>2</sub> devices, it has even been found that the ‘lower quality’ poly-crystalline material has a higher performance than its single crystal counterpart [111, 108]. Theoretical studies of the electronic properties of the grain boundaries in CuInSe<sub>2</sub> have provided an explanation for this unusual observation based on beneficial band offsets at the grain boundaries [100, 101]. This effect is a special case for this particular material, but it embodies the general ideology of thin-film technology well - namely to produce materials able to convert sunlight into electricity as efficiently as possible with the simplest synthesis techniques possible. However typically the efficiencies of second-generation solar cells are less than that of the best performing first-generation devices. Examples of commercial thin-film technologies include CIGS ( $\text{Cu}(\text{In},\text{Ga})(\text{S},\text{Se})_2$ ) and CdTe and figure 1.7 shows that the best performing Si devices have higher efficiencies, which are also much closer to their theoretical limit, than these second-generation, thin-film technologies. Third-generation PV technology aims to make use of the low cost fabrication techniques of the second-generation devices but use multiple energy threshold devices to overcome the Shockley-Quieser limit for a single band gap solar cell, such as in tandem solar cells where semiconductor p-n junctions of increasing band gap are placed on top of each other in order to capture more of the solar spectrum. Typically the more complicated device architecture of

third-generation devices result in higher fabrication costs. Research efforts are therefore largely focused on reducing the fabrication cost of multi-junction devices [142].

Current mainstream solar cell technologies, such as first-generation Si wafers and second-generation thin-film CdTe and CIGS solar cells, would not be able to provide solar electricity at the terawatt scale due to the scarcity of Te and In and the relatively long energy payback time for crystalline Si due to the cost and energy intensive fabrication of Si wafers [143]. Models have even quantified such statements with a predicted In-constrained growth potential of power generation from CIGS PV technology of 20 GW per year in 2020 due to competing applications of In, such as in liquid crystal displays [41]. In order to significantly increase the contribution of solar power to global power consumption, it is therefore necessary to develop more economically viable earth-abundant materials for sustainable PV electricity generation. Furthermore, there must be considerable technological breakthroughs that would enable low-cost manufacturing of highly efficient devices with enough of a cost benefit to outweigh the initial cost outlay in optimizing the manufacturing process of the whole device as has been done for silicon over the past 60 years. For this purpose, there is a drive for solar absorber materials with more optimal properties, such as a direct and sunlight matched band gap (as in thin-film technologies such as CdTe and CIGS), but also for materials that are composed of only earth-abundant components.

## 1.2 The Role of Computational Modelling in Material Design

The discovery of new functional materials by experimental methods is largely hindered by high costs and time-consuming synthesis procedures [31]. However, with the rapid increase in computational processing power and the availability of large-scale supercomputers, we are entering a very exciting era in computational materials design. There are two main contributions that computational simulations could make towards the technological breakthroughs needed for the development of photovoltaic devices for economically-viable, large-scale solar energy

generation. Firstly by predicting properties and screening for certain desirable properties for a solar absorber material, such as an optimal band gap and high carrier mobility, materials simulations are able to aid in the discovery of new materials for use in photovoltaic devices. Secondly, material simulations are able to provide valuable insight to improve understanding of known photovoltaic materials to enable the synthesis of better performing devices. So far in this study we have aimed to make both of these contributions to the field. Firstly, we perform simulations to understand the performance bottlenecks in the candidate earth-abundant, non-toxic solar absorber material Cu<sub>2</sub>ZnSnS<sub>4</sub>(CZTS) and we also study the optical properties of three candidate photovoltaic materials which have so far received little attention as solar materials but could provide another possible route for high-performance photovoltaic devices for cost-effective solar energy generation.

## 1.3 Overview of this Study

### 1.3.1 Promising Candidate Solar Absorber Materials

Refer to: CH 5 (other PV materials) + pg 187 (future of PV) [46]

As already discussed, to make solar energy generation on a large scale economically viable, it must be possible to make devices with an LCOE that is comparable to fossil-fuel resources. Furthermore, the materials that make up the devices must also be sufficiently abundant such that there would be enough to make a substantial number of devices in the first place. For this reason there is a drive for photovoltaic materials that could be made using the low-cost methods associated with second-generation technology, but containing only earth-abundant components. Gauging the abundance of a given material is not as trivial a process as looking at crustal abundance as supply, demand, geographical distribution and extraction must all be considered. However, knowledge of solar cell technologies made from various different materials opens up the possibility of utilizing multiple different materials to collectively contribute to the

global solar power capacity to enable larger-scale power generation from this renewable, low-carbon resource. Additionally by studying various different materials, the scientific community could eventually discover a select few that have the best properties to enable low-cost synthesis of highly efficient devices to eventually significantly reduce the LCOE of solar power.

Presently, two of the most studied candidate earth-abundant thin-film solar cell materials include  $\text{Cu}_2\text{ZnSnS}_4$  (CZTS) and methylammonium lead iodide ( $\text{CH}_3\text{NH}_3\text{PbI}_3$  or  $\text{MAPbI}_3$ ) [143]. The potential of CZTS for photovoltaic applications was realised in 1988 by Ito and Nakazawa [64]. The band gap of the material has been predicted [154] and measured [116] to be 1.5 eV, which corresponds to a theoretical conversion efficiency limit of 28% as predicted by Shockley-Quiesser [119]. However, the current record device efficiency is 8.8% [128] and it is believed that this figure must be increased to at least 15% for the devices to be commercially viable [122]. PV devices composed of a CZTS absorber layer are hampered by low open circuit voltage ( $V_{OC}$ ) [122], which is believed to be due to the formation of secondary phases [7] and defects [26] in CZTS, although the exact origin of the low  $V_{OC}$  remains unknown. The first component of this study is therefore an attempt to determine possible origins of this deficit in CZTS.

$\text{MAPbI}_3$  is an example of a hybrid halide perovskite solar cell material, which are regarded as a convergence of inorganic thin-film and dye-sensitised solar cells (DSSC's) [19]. Research on such materials dates back to 1928 [141]. The efficiency of  $\text{MAPbI}_3$  solar cells however has increased rapidly between 2009 and 2014 from 3.8% for  $\text{MAPbI}_3$ -based DSSC's to 20.1% for a planar  $\text{MAPbI}_3$ -based thin-film solar cells [143] and has therefore surpassed the record efficiency of both conventional DSSC's as well as the earth-abundant thin-film PV absorber material CZTS [19]. Electricity generation in a typical PV device, such as that shown in the schematic in figure 1.4, is dependent upon charge separation by variation in material composition, as in a p-n junction. However, in ferroelectric materials charge separation can also be achieved due to the intrinsic crystal field in a homogeneous material. The crystal polarity creates microscopic electric fields across domains, separating photogenerated excitons into free charges, and segregating the transport of the free charges to reduce recombination rates [23]. Hybrid perovskites

have been shown to exhibit spontaneous electric polarization [40]. Therefore, one possible explanation for the high efficiency of MAPbI<sub>3</sub>-based solar cells is enhanced separation of photoexcited electron and hole pairs, and hence reduced rate of electron-hole recombination, due to the presence of ferroelectric domains [40, 19]. Although the stability of MAPbI<sub>3</sub>-based solar cells has been identified as a big challenge for these devices, as CH<sub>3</sub>NH<sub>3</sub>PbI<sub>3</sub> is very sensitive to polar solvents such as water and so readily dissolves and decomposes into PbI<sub>2</sub> [99].

A number of interesting PV phenomena have been observed in ferroelectric (FE) materials such as the bulk photovoltaic effect (BPE) and the anomalous photovoltaic effect (APE) [23]. Ferroelectric materials usually have a high dielectric constant (which was mentioned in section 1.1.3 as an important parameter for a photovoltaic material) and they possess a spontaneous electric polarization that can be switched between two or more states using an electric field [81]. The BPE was first recorded in 1956 in BaTiO<sub>3</sub> [29], where photovoltages were measured in un-doped single crystals [23]. The BPE effect is distinctly different from the typical PV effect in semiconductor p-n junctions as it is the polarization electric field that is the driving force for the photocurrent in FE-PV devices [150]. The APE was first observed in PbS films in 1946 [125] and has since been reported in polycrystalline CdTe, ZnTe, InP [69, 49, 135], where photovoltages output along the polarization direction can be significantly larger than the band gap of the material [150], which is usually the limit for a semiconductor PV material [23]. The Shockley-Queisser limit, which prevents any single p-n junction solar cell from converting more than 33.7% of the incident light into electricity, has not been predicted to apply for these photovoltaic phenomena. An upper limit for the theoretical power conversion efficiency (PCE) from this photovoltaic mechanism seems to still be an open question [97], although an ultimate maximum efficiency of any single-band gap absorber of 44% has been set by thermodynamic considerations [119]. Theories to explain the PV phenomena observed in FE materials are discussed further in section 2.6.2.

The identification and understanding of such phenomena may open up the possibility of more efficient PV devices constructed from a number of different photoferroelectric materials. How-

ever, most of the commonly used ferroelectric materials such as LiNbO<sub>3</sub> and BaTiO<sub>3</sub> have band gaps larger than 3 eV and can therefore only absorb sunlight in the UV range to convert into electricity, which accounts for only around 3.5% of the solar spectrum [150], which is illustrated in figure 1.6. The optimal range for the band gap in order to absorb the majority of the solar spectrum under typical radiation conditions is between 1.06 eV and 1.50 eV [63]. Research efforts have also gone into adjusting the optical absorption of ferroelectric materials without influencing the ferroelectric properties of the material through chemical doping or alloying [150]. In Bi<sub>4</sub>Ti<sub>3</sub>O<sub>12</sub> (BiT) the optical band gap has been tuned in such a way, resulting in a decrease from 3.6 eV to 2.7 eV [28], although this is still considerably larger than the optimal range for a PV absorber material.

This then leads on to the second component of this study, which is an investigation of the optoelectronic properties of new candidate solar absorber materials that may also exhibit ferroelectricity, but have band gaps within the optimal range for the absorption of sunlight. In theory, these materials may exhibit the exceptionally high performance of MAPbI<sub>3</sub>-based solar cells (ideally without the instability issues suffered by MAPbI<sub>3</sub>) or enable the possibility of exploiting other novel photovoltaic phenomena such as the anomalous and bulk photovoltaic effects to overcome the Shockley-Quiesser efficiency limit without the need for such complicated device architectures as in third-generation tandem solar cells. Although the difference between the Shockley-Quiesser limit and the ultimate thermodynamic limit of a solar material is not enormous, it is also possible that ferroelectric materials have properties that enable more efficient devices to be made more easily, such as good screening of the effect of defects due to a high dielectric constant or enhanced electron-hole separation from ferroelectric domains resulting in reduced recombination and a higher performance solar cell with ‘low quality’ defective and nanostructured materials. Such technologies could provide one possible route for the technological breakthrough that could enable economically-viable, large-scale solar energy generation.

### 1.3.2 Investigating Possible Performance Bottlenecks of Cu<sub>2</sub>ZnSnS<sub>4</sub> Devices

\*\* Check against Laurie's April highlights (top two bullet points on disorder)

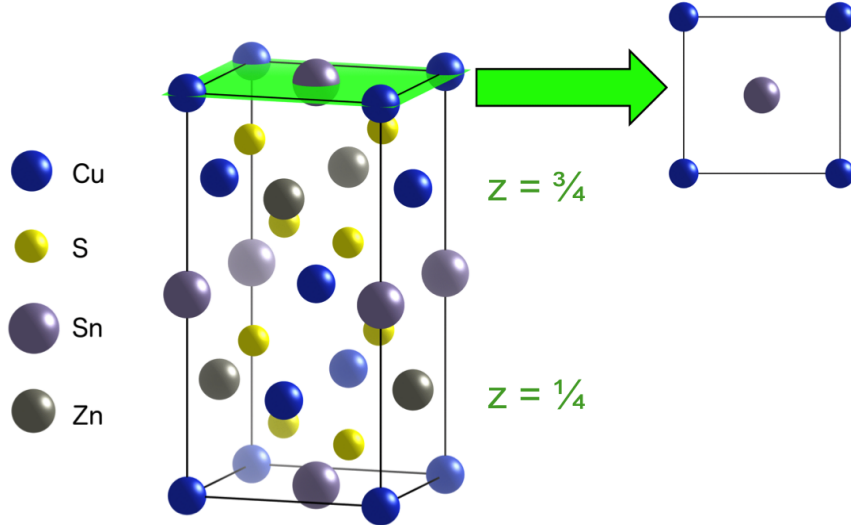


Figure 1.11: The conventional unit cell of CZTS (Cu<sub>2</sub>ZnSnS<sub>4</sub>) with the ground-state kesterite crystal structure (space group  $I\bar{4}$ ). The structure consists of alternating layers of Cu-Sn and Cu-Zn where Cu-Zn layers are at  $z=\frac{1}{4}$  and  $z=\frac{3}{4}$ .

The ground state crystal structure of CZTS (Cu<sub>2</sub>ZnSnS<sub>4</sub>) is kesterite (space group  $I\bar{4}$ ). The conventional unit cell of CZTS is shown in figure 1.11, where each S is surrounded by two Cu, one Zn, and one Sn to satisfy local charge neutrality and the valence-octet rule. Kesterites meet two necessary conditions for highly efficient solar cells, which are a band gap that is both direct and relatively well-matched to the solar spectrum [63]. Over the last decade the power conversion efficiency of PV devices based on kesterite, Cu<sub>2</sub>ZnSn(S<sub>x</sub>Se<sub>1-x</sub>)<sub>4</sub> (CZTSSe), compounds has improved greatly from around 5% in 2004 to 12.6% in 2013 [1]. However, this is still far from the record efficiencies of Cu(In<sub>1-y</sub>,Ga<sub>y</sub>)Se<sub>2</sub> (CIGSe) devices of >20%, where the materials have very similar band gaps to those of CZTSSe [17] and so should have the same theoretical efficiency limit as predicted by Shockley and Queisser [119]. Furthermore, the rate of improvement seems to have slowed considerably recently with the last improvement in efficiency being reported in 2014 and with only a 0.1% improvement [72]. A large number of possible explanations have

been proposed to explain the current difference in efficiency between CZTSSe and CIGSe devices, many of these are illustrated in figure 1.12. The majority of studies converge towards the low open circuit voltage ( $V_{OC}$ ) relative to the band gap, i.e. the  $V_{OC}$  deficit, being the main limiting factor on device performance. As can be seen from the position of CZTSSe devices on the plot in figure 1.13, the open circuit voltages measured for these devices are considerably less than that of a CIGS device, which has a similar value for the band gap of the material.

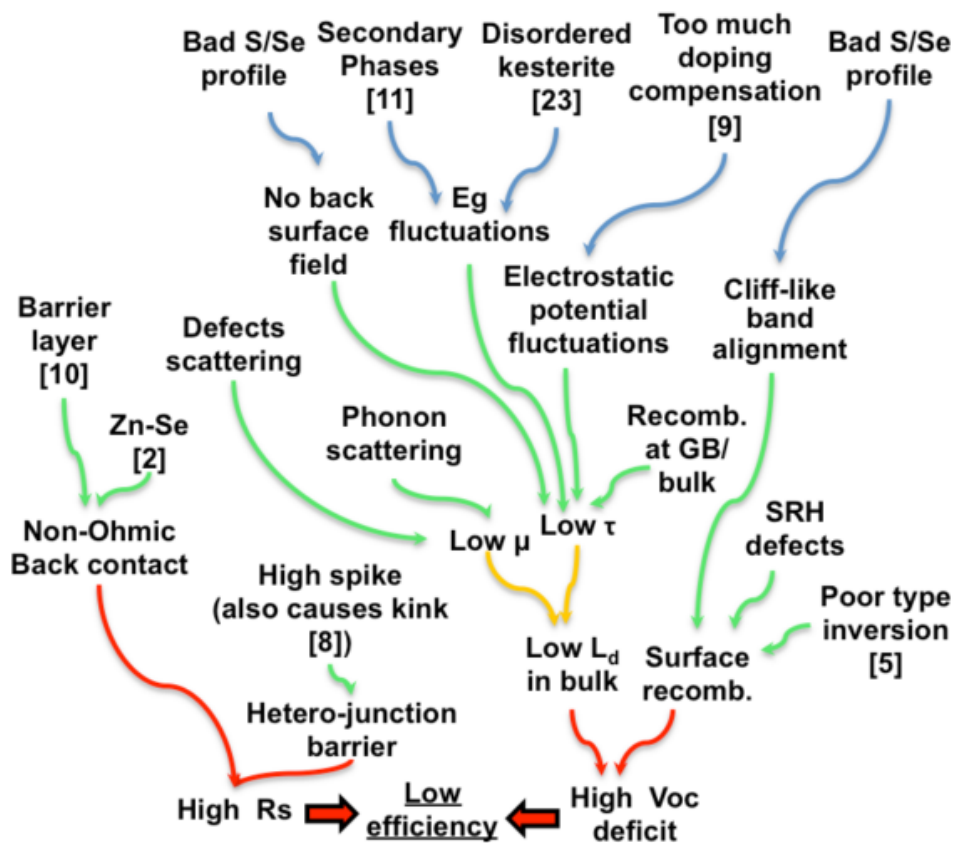


Figure 1.12: Mapping of the numerous possible mechanisms limiting the efficiency in kesterite devices and their possible causes.  $R_s$  is the series resistance between the absorber layer and back contact of the device and  $V_{OC}$  is the open circuit voltage across the absorber layer. Figure taken from 30.

As figure 1.12 shows, there are many different possible causes of the  $V_{OC}$  deficit in kesterite solar cells. Developing fabrication techniques to reduce the deficit is therefore an even greater challenge when the exact cause is not yet known. This is an area in which computational materials simulations should be able to provide valuable insight to help pinpoint the specific sources of the  $V_{OC}$  deficit in kesterite solar cells. The true power of simulation is the ability to take a

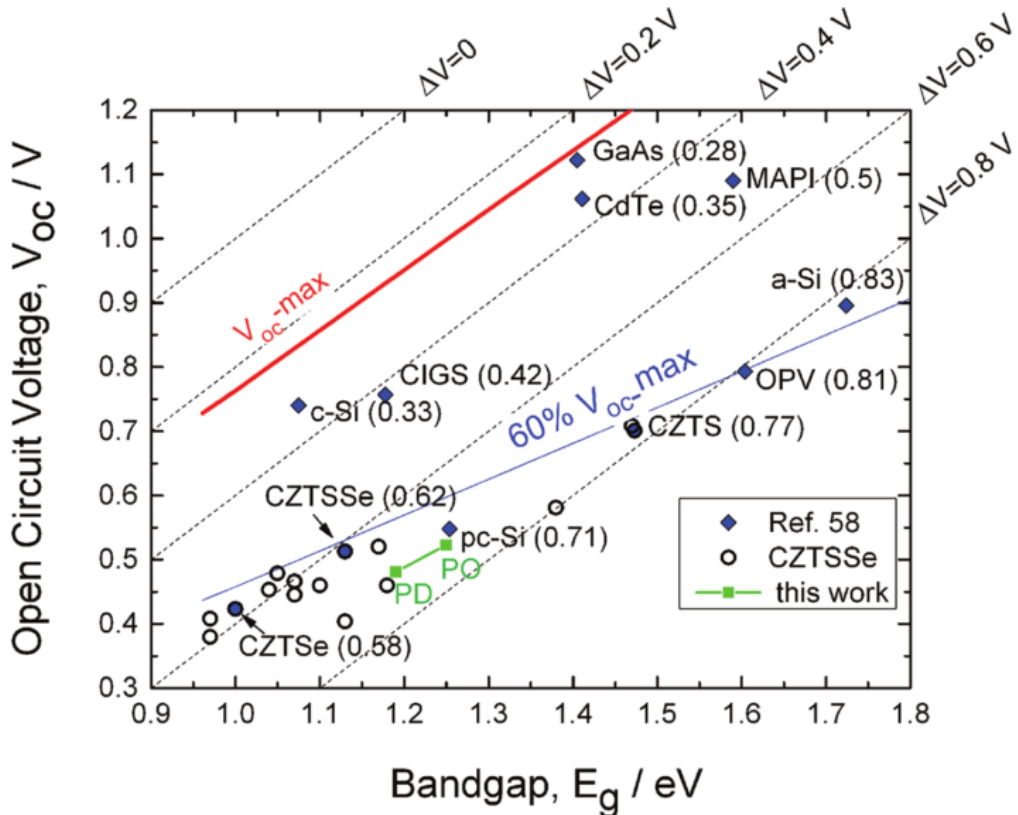


Figure 1.13:  $V_{OC}$  versus band gap of high performance CZTSSe devices ( $>9\%$  efficiency) indicated by circles with best devices based on other photovoltaic materials shown for comparison by diamond symbols: Methyl-ammonium lead iodide (MAPI), amorphous silicon (a-Si), organic photovoltaic films (OPV), crystalline silicon (c-Si) and polycrystalline silicon (pc-Si). The oblique lines give a constant  $V_{OC}$  deficit from 0.8 V to 0 V. The green points correspond to CZTSSe films that are partially ordered (PO) or partially disordered (PD) due to disorder amongst Cu and Zn. Figure taken from reference 17.

perfect system and introduce various imperfections one at a time and then study the effect that particular imperfection could have on device performance. As opposed to in a real system in which there is a myriad of possible causes for each observation, as illustrated in figure 1.12. In our simulations we will start from the most simple system possible, before making any attempts to build up in complexity. Devices made from a compound of  $\text{Cu}_2\text{ZnSnS}_4$  and  $\text{Cu}_2\text{ZnSnSe}_4$ , i.e.  $\text{Cu}_2\text{ZnSn}(\text{S}_x\text{Se}_{1-x})_4$ , so far have given the highest performance devices, however in this study we are currently focusing on just the pure selenide material, CZTS. In addition to simplifying the system, figure 1.13 also indicates that the  $V_{OC}$  deficit is worse in purely CZTS devices and so potentially studying causes of the problem in this particular system could be more informative. Also although ultimately the aim is to make thin-film devices from CZTS, in which

the material is likely to be highly polycrystalline with many grain boundaries, we are currently just focusing on the bulk material. We are doing this for two reasons. Firstly to improve the understanding of the fundamental material properties before attempting to understand a more complex system to ensure we start from a solid foundation. Secondly, it has been proposed that the  $V_{OC}$  deficit in CZTSSe devices could actually be largely due to the natural bulk properties of the crystal [103]. For the purposes of our study therefore measurements performed on single crystals will be the most directly relatable to our findings, wherever the data is available.

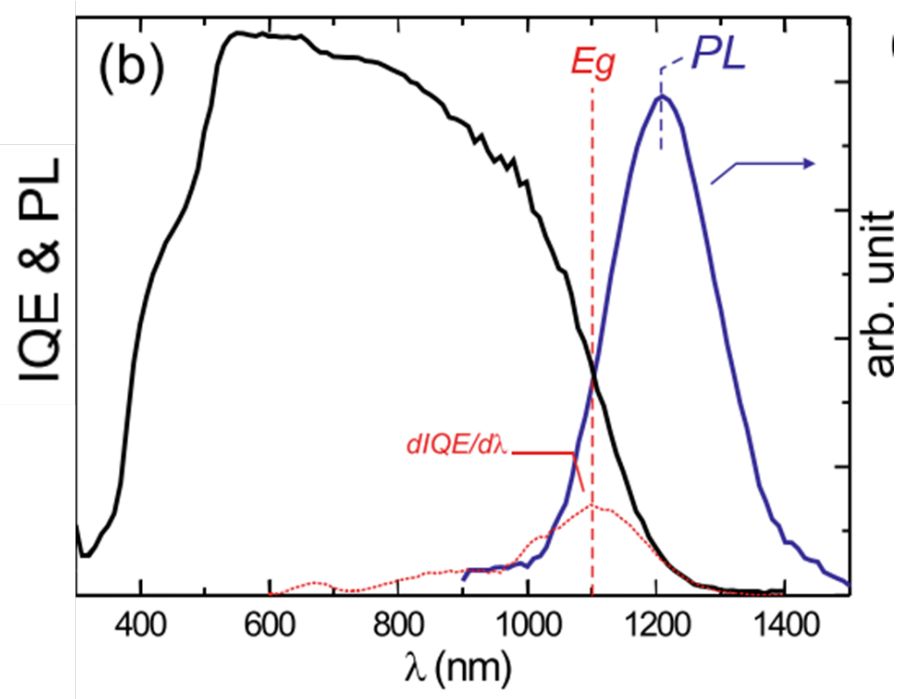


Figure 1.14: Internal quantum efficiency (IQE) and photoluminescence (PL) spectra of CZTSSe thin-films showing the shift of the PL peak to energies below the band gap of the material. Figure taken from reference 47.

In general, the main cause of  $V_{OC}$  deficit in a PV device is the recombination of photogenerated charge carriers in the bulk material or at surfaces [17]. Figure 1.14 shows photoluminescence (PL) spectroscopy measurements performed on CZTSSe thin films by Gokmen et al [47]. The emission spectra of semiconductors is discussed much more thoroughly in section 2.5.2 and a review of various PL studies performed on kesterite thin films and crystals is given in section 2.5.3, but for current purposes the key observation to be made from figure 1.14 is that there is a shift in the PL peak to lower energies (red-shifting), below the value of the band gap obtained

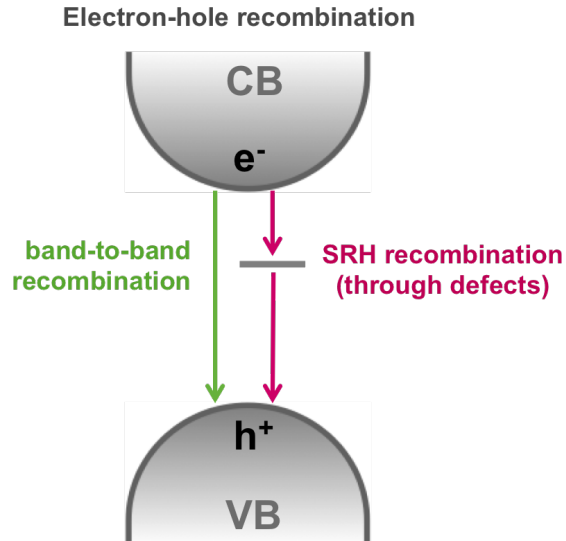


Figure 1.15: Illustration of Shockley-Read-Hall (SRH) electron-hole recombination due to energy states introduced into the band gap by defects.

from internal quantum efficiency (IQE) measurements performed on the same thin films. It is also noted in this study when comparing the PL spectra of CZTSSe films to that of CIGSSe films that the PL peak for CZTSSe thin films is broader and that the red-shifting was roughly twice as severe. This effect is referred to as ‘band-edge tailing’, where photons of energies less than the band gap of the material are emitted following photoexcitation and subsequent relaxation back to the ground state. This effect is known to be detrimental for device performance as emitted photons may then not have sufficient energy for subsequent photoexcitations in the absorber layer, the energy of the original photon may then not be converted into electricity if the photoexcited electron-hole pair recombine before the charge is collected [88]. Band tailing and the possible causes of this detrimental effect are discussed further in section 2.4, but for now it is worth briefly noting that possible causes are: Shockley-Read-Hall recombination due to defect-induced mid-gap states [120], as illustrated in figure 1.15, as well as fluctuations in electrostatic potential due to the presence of charged defects and fluctuations in the band gap of the material due to an inhomogeneous composition [47], which are both shown in figure 1.16.

The extent of band tailing due to the additional energy levels introduced into the band gap of a material by particular intrinsic defects is dependent upon the concentration of those particular defects. The equilibrium defect concentration can be obtained directly from the defect forma-

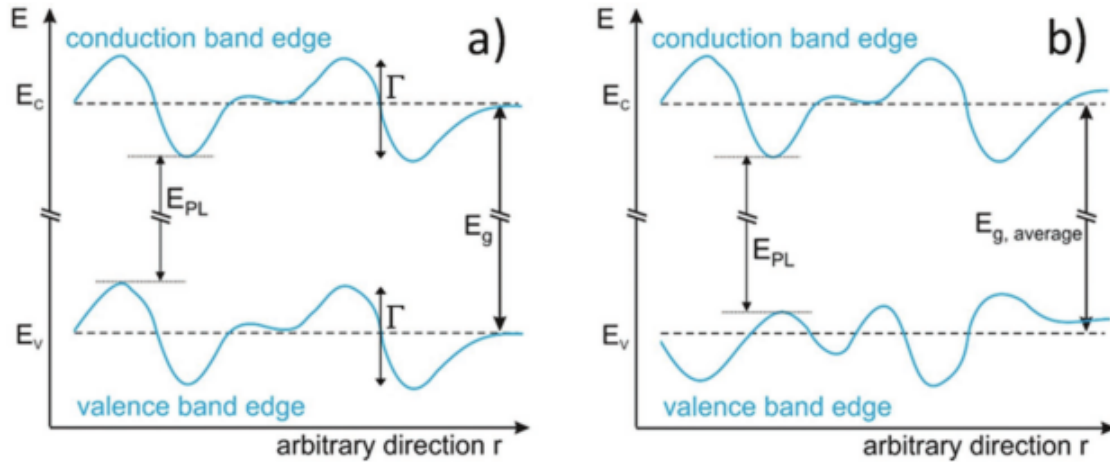


Figure 1.16: The effect of electrostatic potential fluctuations (a) and band gap fluctuations (b) on the electronic bands of a semiconductor. In both cases radiative transitions at energies below the (average) band gap are possible. The band gap in a is constant and not affected by local charged defects, while band edges in b can differ depending on e.g., long range composition variations. Figure taken from reference 17.

tion energy [90], which is discussed further in section ???. For materials such as CZTSSe that are still at a fairly early stage of development, theoretical predictions of defect formation energies may be the only values available to help identify specific defects and their properties in real systems [73]. Theoretical predictions for the formation energies and depth of defect-induced energy levels for various intrinsic point defects and defect clusters in CZTS made by Chen et al [27] are shown in figures 1.17, 1.18, 1.19 and 1.20. Based on the predictions made by Chen et al, figure 1.18 shows that many of the intrinsic defects involving Sn would induce a mid-gap state, however figure 1.17 shows that the formation energy of those particular defects would all be expected to be high. It therefore would be expected that these defects are less likely to form and should be present in lower concentrations than other defects. Although other works have suggested that the formation of this defect could be more likely if it forms part of a particular defect cluster [139, 17]. From the work by Chen on defect clusters, it is also expected that certain charge compensated defect clusters would have very low formation energies, in particular the  $[Cu_{Zn}^- + Zn_{Cu}^+]$  antisite defect pair, as shown in figure 1.19.

Disorder amongst Cu and Zn ions (or equivalently the formation of the  $[Cu_{Zn}^- + Zn_{Cu}^+]$  antisite defect pair) in CZTS has been proposed as one possible origin of the  $V_{OC}$  deficit in CZTS

and consequently a number of experimental studies have been conducted to investigate this [115, 113, 37, 112]. Additionally it is worth noting that this substitutional disorder does not exist in the crystal structure of CIGSe due to the considerably larger chemical mismatch between Cu with In or Ga [17], whereas Cu and Zn are so similar that disorder between the two species can be difficult to detect experimentally. As Cu and Zn are neighbouring elements in the periodic table, the changes in the bonding between the two are subtle [85]. This results in a theoretical energy difference between the two structures of just 3 meV per atom [25] allowing for intermixing of the Cu and Zn cations in CZTS, which has been confirmed by neutron diffraction [113, 37] and also measured using near resonant raman scattering [115]. However, a recent work prepared samples with varying degrees of Cu-Zn disorder (by varying the cooling rate during synthesis, which had been shown in a previous study to have a considerable effect on Cu-Zn ordering in CZTS [115]) and in this work they showed that a reduction in Cu-Zn order resulted in a reduction in both the band gap and  $V_{OC}$ , thereby not influencing the  $V_{OC}$  deficit relative to the band gap of the material [17].

In this work we begin three investigations to explore some of the possible explanations for the  $V_{OC}$  deficit in CZTS solar cells and to attempt to explain the PL spectra of CZTS shown in figure 1.14. As discussed above, intrinsic defects can introduce additional energy levels into the band gap of the material and energy states within the band gap are Shockley-Read-Hall recombination sites [120]. We re-investigate the formation energy of sulfur vacancies ( $V_S$ ) in CZTS. This is another possible deep donor defect in CZTS and it was proposed in a recent study using admittance spectroscopy measurements performed on CZTSSe, combined with electrical modelling, that in addition to majority p-type defects in CZTSSe (giving the material its p-type conductivity), there may also been deep n-types defects [139].  $V_S$  in CZTS has been predicted to produce a mid-gap state in the band gap of the material [27], which could provide one explanation for the poor device performance. However in the same work this particular point defect was also predicted to have a high formation energy relative to other possible intrinsic defects, making it less likely to form. However, it is possible that the formation energy of this defect is reduced when considering the typical annealing conditions of CZTS in which S is in the gaseous phase. We therefore calculate the formation energy of a  $V_S$  in CZTS as a function

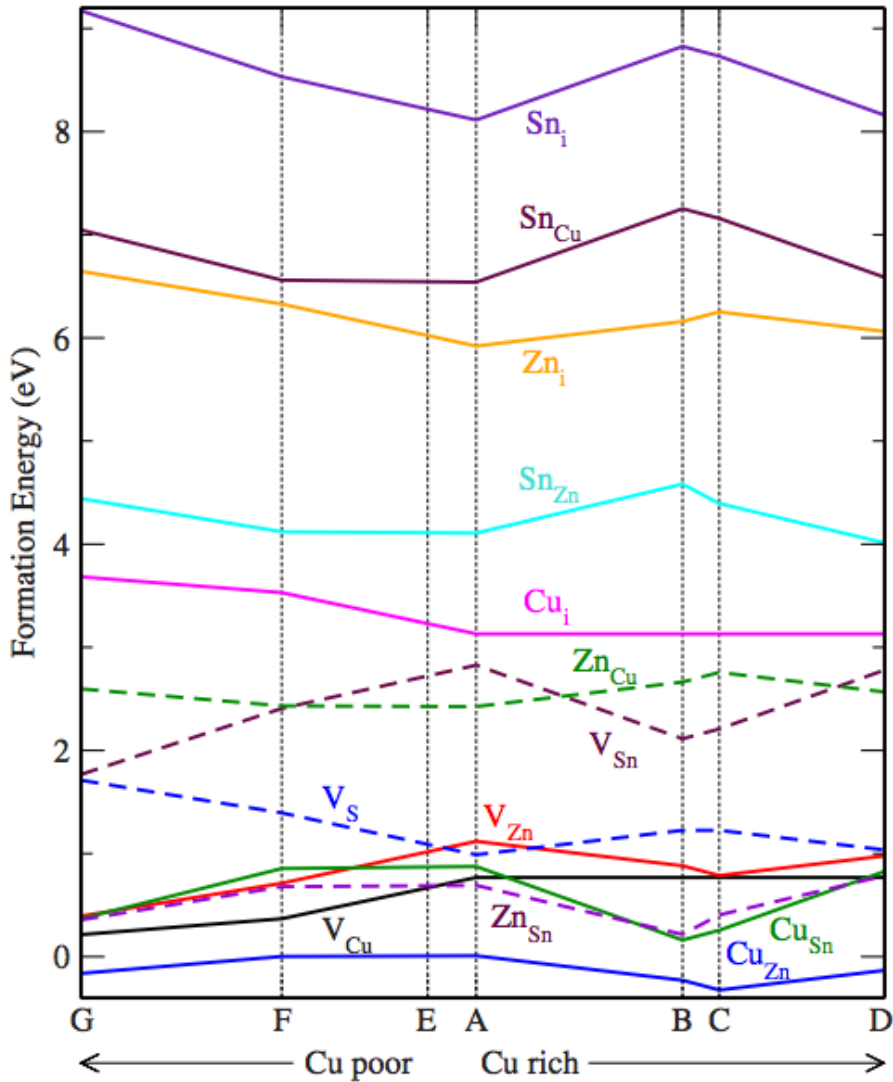


Figure 1.17: The formation energy of neutral intrinsic defects in  $\text{Cu}_2\text{ZnSnS}_4$  as a function of the chemical potential. Figure taken from reference 27.

of the sulfur chemical potential, which has been calculated as a function of temperature and pressure in a previous study [65], making it possible for us to compare directly to experimental synthesis conditions.

Secondly, we examine possible causes of band gap broadening, which has been observed in electromodulation (?) measurements performed on CZTS crystals [? ]. We use materials modelling to determine the intrinsic band gap broadening to be expected even in perfect, bulk CZTS due to thermal lattice expansions. This contribution can then be subtracted from band

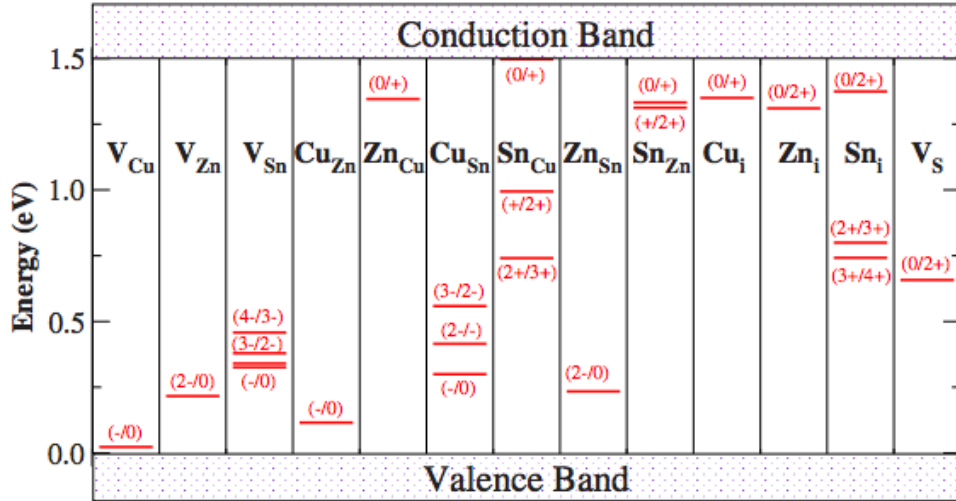


Figure 1.18: The transition-energy levels of intrinsic defects in the band gap of  $\text{Cu}_2\text{ZnSnS}_4$  where the GGA band gap has been corrected to the experimental value 1.5 eV, and the donor levels are shifted together with the conduction band minimum (CBM) level. Figure taken from reference 27.

gap broadening measured experimentally to determine how much of this effect is due to disorder and other factors. Lastly, we simulate thermodynamic substitution amongst Cu and Zn ions in CZTS and study the resulting changes in the distribution of electrostatic potential in the system in an attempt to extract the contribution of this particular type of disorder to the strong band tailing that has been observed in kesterite devices, which has been suggested to be due to fluctuations in electrostatic potential [47]. As discussed above, disorder amongst Cu and Zn ions has not only been predicted to be very likely based on energetics but has also been observed experimentally, it would therefore be important to know if this particular type of disorder is having a detrimental effect on device performance or to at least eliminate it from the list of many possible causes of the  $V_{OC}$  deficit.

\*\*Edit last paragraph once PVTEAM paper published so have more info + put eris study first to match order of results?\*\*

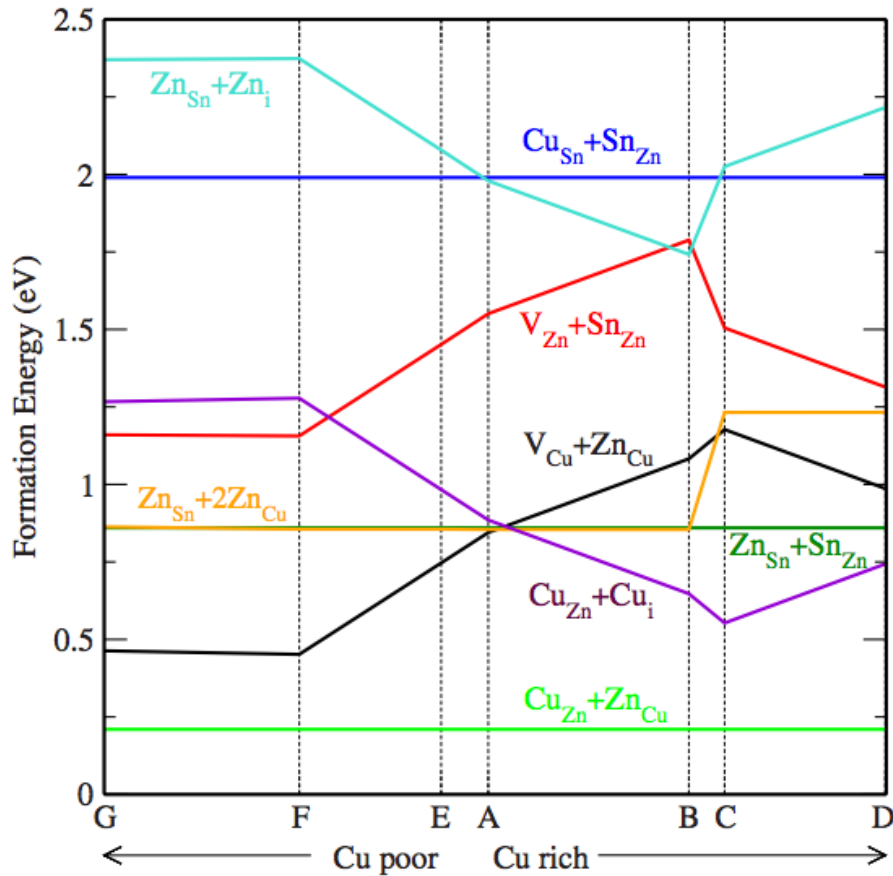


Figure 1.19: The formation energy of charge compensated defect complexes in  $\text{Cu}_2\text{ZnSnS}_4$  as a function of the chemical potential. Figure taken from reference 27.

### 1.3.3 Predicting the Properties of New Candidate Solar Absorber Materials

The second part of this study involves using materials modelling to predict the optoelectronic properties of materials that could have the potential to be used to produce high performance PV devices, but until now have received little research interest for applications in PV. The central idea in selecting these candidate materials was to identify any that may be ferroelectric and so could exhibit some of the novel FE-PV phenomena discussed earlier but may also have a band gap within the optimal range for solar absorption. Photoferroelectric, or photoferroic, is the name given to materials that exhibit such properties. Using very simple screening criteria, we identified three candidate photoferroelectric solar absorber materials from a data set of over 200 naturally occurring minerals. A dark-coloured material suggests (but does not guarantee)

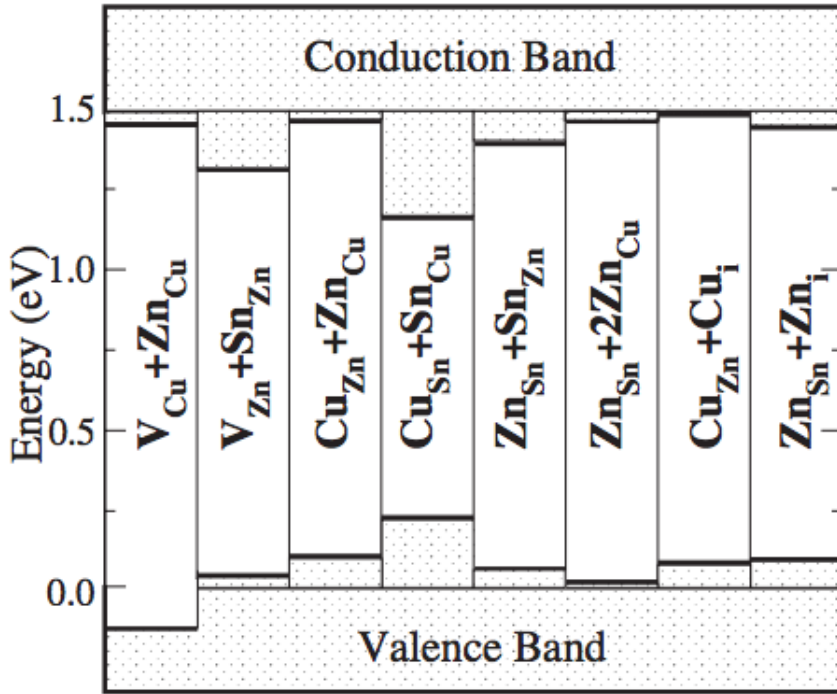


Figure 1.20: The conduction band minimum (CBM) and valence band maximum (VBM) levels in eV of  $Cu_2ZnSnS_4$  with different charge-compensated defect complexes relative to the host material at 0 eV and 1.5 eV respectively. Figure taken from reference 27.

that it absorbs light in the visible range. Ferroelectric materials are a subset of materials with polar crystal structures, therefore not all polar materials exhibit ferroelectricity. It is only polar materials that also possess a spontaneous electric dipole moment within the unit cell which can be inverted by the application of an external electric field that exhibit ferroelectricity [32]. Therefore, the conditions used to screen for candidate photoferroelectric materials shown in the Venn diagram in figure 1.21 are necessary conditions for photoferroelectricity, but cannot guarantee this property as a polar space group is a necessary but not sufficient condition for ferroelectricity. The three candidate photoferroelectric materials identified by our screening process were: enargite ( $Cu_3AsS_4$ ), stephanite ( $Ag_5SbS_4$ ) and bournonite ( $PbCuSbS_3$ ). All three minerals are sulfosalts, which are materials that contain two or more metals, semi-metals such as antimony and arsenic, and sulfur [16].

Scientific research on sulfosalts has largely focussed on the thermodynamic properties and crystal structure of the materials, leaving knowledge of the optoelectronic properties of sulfosalts

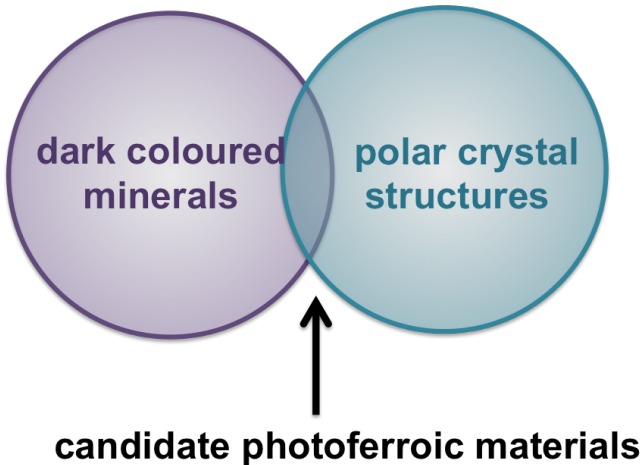


Figure 1.21: Venn diagram showing the necessary (but not sufficient) conditions for a material to exhibit photoferroelectricity, where the dark colour suggests absorption of light in the visible range and a polar crystal structure is a requirement (but does not serve as a guarantee) for a material to exhibit ferroelectricity.

relevant for PV applications extremely scarce. The potential of sulfosalt minerals for PV applications however was highlighted by Dittrich et al in 2007 [33]. This work also provides an overview of thin film deposition methods that have been developed for sulfosalt layers and discusses a 1% efficient Sn-Sb-S sulfosalt thin film solar cell constructed by the authors. The thin film deposition methods discussed for other sulfosalt materials would also be particularly important for the eventual aim of constructing PV devices from these materials. The potential of the sulfosalt mineral enargite for PV applications has been suggested even earlier by Pauperté and Lincot in 1995 [98]. In addition to synthesis methods, another important consideration for the large-scale deployment of solar devices composed of the candidate materials is the price and abundance of the elemental components. Figure 1.22 shows a comparison of the price and abundance of some of the elemental components of the three candidate materials: Cu, Sb and S, to that of elements used in some current commercial thin film solar cell absorber materials such as CuIn(Ga)Se<sub>2</sub> (CIGS) and CdTe. The components of the candidate materials not included in the figure are As, Pb and Ag. Lead can be considered as the most abundant and universally diffused metal after iron. Although it is never found in the native state, its ores are very numerous [130]. 5,200,000 tonnes of lead was produced in 2012 [134], although its crustal abundance is considerably smaller than that of iron being around 10-14 ppm to compared to approximately 60,000 ppm for iron [114]. Silver and arsenic are both fairly abundant metals.

Silver often occurs in combination with lead, copper, iron, antimony and tellurium. Arsenic is also present in most ores of silver [130]. The crustal abundance of arsenic is approximately 1.5 ppm and that of silver is relatively low at approximately 0.070 ppm [114]. These values are however still larger than that of indium (0.049 ppm [114]), which is also in demand for the display industry [122].

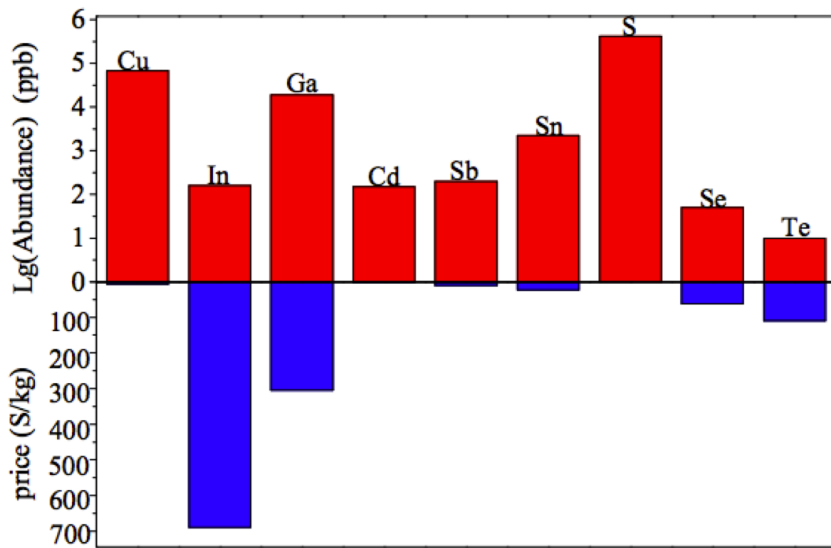


Figure 1.22: Comparison of element abundance and price between Cu, In, Ga, Cd, Sb, Sn, S, Se and Te. Figure taken from the supporting information of reference 144, where data was taken from the London Metal Exchange LME.

The first candidate photoferroelectric material, enargite ( $\text{Cu}_3\text{AsS}_4$ ), is a mineral that corresponds to a semiconductor of type  $A_3^I B^V C_4^{II}$ , and is frequently found as an impurity in copper ores [136]. Minerals of the composition  $\text{Cu}_3(\text{As}, \text{Sb})\text{S}_4$  are known to occur in two polymorphs: tetragonal with sulfur in cubic close packing or orthorhombic with sulfur in hexagonal close packing. In both cases the coordination is tetrahedral for all atoms [121]. Enargite is the most common member of this group of minerals, its unit cell (as shown in figure 1.23a) has an orthorhombic crystal structure with space group  $Pmn2_1$  and chemical composition  $\text{Cu}_3\text{AsS}_4$  with a small percentage of Sb [83]. The main impurities in natural enargite are Sb and Fe, but Pb and Ag are also known to be present to some extent [136]. Natural samples of enargite have been found to exhibit the electrical properties of a p-type doped semiconductor with a

conductivity of 0.0014 S/m (from the stated value of approximately  $7 \Omega \text{ cm}$  for the resistivity at 295 K) [98]. In the same work, two optical transitions were determined: an indirect one at 1.19 eV and a direct one at 1.44 eV. Although more recent studies have given a value of 1.28 eV for the band gap of enargite from measurements of temperature dependent resistivities, diffuse reflectance spectroscopy and photoacoustic spectroscopy [34]. A theoretical study using the first principles quasi-particle GW method based on wavefunctions generated from the hybrid functional HSE06 [54], has predicted a value of 1.32 eV for the band gap [148]. Although a number of different values have been reported for the band gap of enargite, all values stated fit within the optimal range of 1.06 eV to 1.50 eV [63] for a solar absorber material.

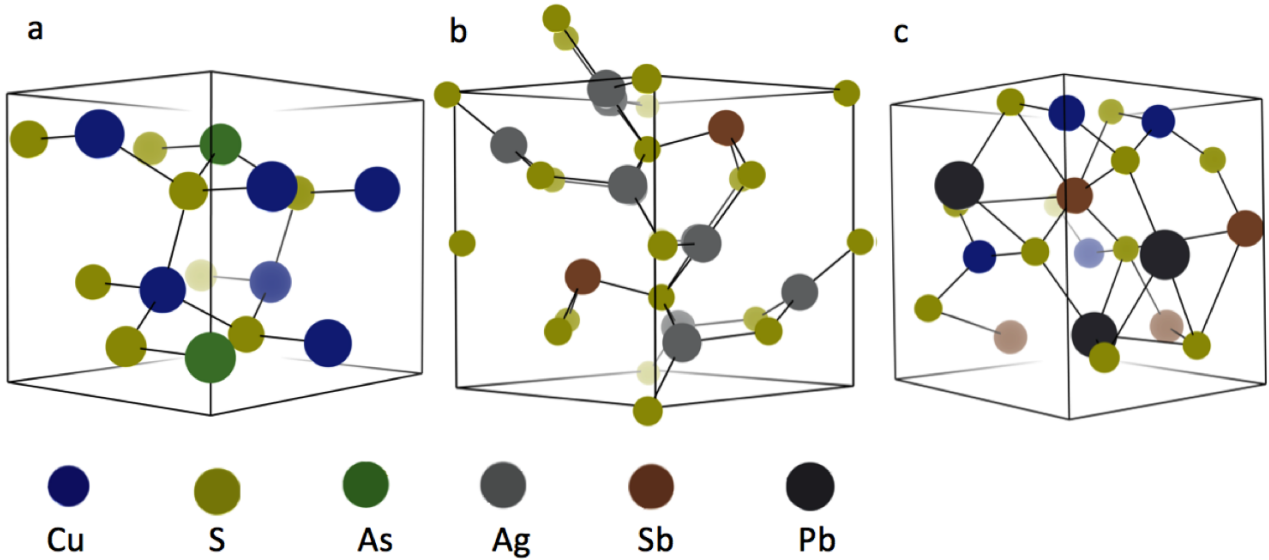


Figure 1.23: The 15 atom primitive unit cell of enargite ( $\text{Cu}_3\text{AsS}_4$ ) (a), 19 atom primitive unit cell of stephanite ( $\text{Ag}_5\text{SbS}_4$ ) (b) and 23 atom primitive unit cell of bournonite ( $\text{PbCuSbS}_3$ ) (c).

The unit cell of the second candidate photoferroelectric material, stephanite ( $\text{Ag}_5\text{SbS}_4$ ), also has an orthorhombic crystal structure but with space group  $Cmc2_1$ , and is shown in figure 1.23b. The structure is composed of columns of  $\text{SbS}_3$  pyramids extended along the z axis. The columns are located pairwise; in each column, pyramids occupied with antimony atoms alternate with empty pyramids. The Sb-S distances in the pyramids are 2.48, 2.42, and 2.42 Å. Silver atoms are located in the tetrahedral coordination between  $\text{SbS}_3$  groups (at the centers of rhombic channels). Three types of  $\text{AgS}_4$  tetrahedra with different Ag-S distances can be identified. The distinctive feature of the structure is a large number of common edges of Ag

tetrahedra [96]. It has been reported that stephanite has a band gap of 1.62 eV [34]. Otherwise, there is seemingly very little information available in the literature on the optical or electrical properties of stephanite apart from a work in 1973, given in reference 24, showing the electrical resistivity of a synthetic sample of stephanite as a function of temperature. The work measures a resistivity of approximately  $9 \Omega \text{ cm}$  for the stephanite sample at  $110^\circ\text{C}$ , which corresponds to a conductivity of 0.0011 S/m. There has also been some speculation in the literature on the possibility of ferroelectric behaviour in stephanite due to the presence of ferroelectric phases at very low temperatures in pyrargyrite ( $\text{Ag}_3\text{SbS}_3$ ), proustite ( $\text{Ag}_3\text{AsS}_3$ ) and stibnite ( $\text{Sb}_2\text{S}_3$ ), which are crystallochemically related to stephanite [96]. The same study also notes that similar displacement structural changes occur in stephanite to those in proustite and pyrargyrite that are responsible for the ferroelectric properties of these materials.

Similarly, up until very recently, little information has been available on the optical or electrical properties of the third candidate photoferroelectric material, bournonite ( $\text{PbCuSbS}_3$ ). Bournonite also has an orthorhombic crystal structure and the same space group as enargite,  $Pmn2_1$ , with measured values of 1.23 eV [34] and 1.31 eV [138] reported for the band gap. However, very recently this material has received increasing scientific interest for thermoelectric and rewriteable data storage applications due to a measured low thermal conductivity [35]. Consequently, works on the synthesis of bournonite are beginning to emerge such as that in reference 138. The low thermal conductivity of bournonite has been attributed to the distortive environment of the Pb and Sb atoms from the stereochemically active lone-pair  $s^2$  electrons [35]. In the same study they perform electronic structure calculations to predict the band structure of the material, however in the study they use only the generalized-gradient approximation (GGA) level of accuracy in density functional theory for their calculations, which is known to underestimate the band gap of a semiconducting material. They do however show that the inclusion of spin-orbit coupling (SOC) has a considerable impact on the calculated band gap of the material. In the study they predict a direct band gap of 0.686 eV before including SOC and two optical transitions when they do include SOC: a direct band gap of 0.445 eV and an indirect band gap of 0.385 eV. Different levels of accuracy in DFT electronic structure

Table 1.1: Summary of known key properties of the three candidate photoferroelectric materials from the literature.

Candidate	Empirical Formula	Space Group	Band Gap (eV)	Conductivity (S/m)
Enargite	$\text{Cu}_3\text{AsS}_4$	$Pmn2_1$	1.28 [34]	0.0014 [98] <sup>ii</sup>
Stephanite	$\text{Ag}_5\text{SbS}_4$	$Cmc2_1$	1.62 [34]	0.0011 [24] <sup>ii</sup>
Bournonite	$\text{PbCuSbS}_3$	$Pmn2_1$	1.23 [34], 1.31 [138]	-

<sup>i</sup> From resistivity of a natural sample measured at 295 K

<sup>ii</sup> From resistivity of a synthetic sample measured at 383 K

calculations and the impact of SOC on the optoelectronic properties of a material are discussed further in sections 3.1.1 and 2.6.1 respectively. A more recent study has made use of DFT+U methodology to avoid the underestimation of the band gap when calculating the optoelectronic properties of this material, where they predicted a band gap of 1.22 eV [127]. There was however no mention of SOC in the study, which was shown in the older study to influence the band structure of the material considerably, and the limitations of DFT+U methodology are discussed in section 3.1.1.

The key known experimentally derived properties of the three candidate materials that were described above are summarised in table 1.1. In this study we aim to use the highest level of theory possible to calculate as many of the properties relevant for a solar absorber material as possible, which were discussed in section 1.1.3, in order to determine if these materials are likely to perform well in this application. Firstly we use hybrid-DFT electronic structure calculations to optimize the crystal structure of a bulk system, starting from the highest quality X-Ray diffraction data available for the materials. From this we calculate the band structures of the materials to determine the size of the band gap and whether it is direct or indirect in nature as this would be a good indicator of how strongly the materials will absorb sunlight. We then go on to calculate the dielectric function and optical absorption coefficients of the materials...

# Chapter 2

## Background Theory

### 2.1 Models of Perfect Periodic Crystal Structures

Refer to: pg 28 29 35 [14]

Theoretical models of crystalline solids are based around the existence of translational symmetry in a crystal lattice such that the lattice can be constructed by periodically repeating a unit cell of atoms. The Bravais lattice specifies the periodic array in which the repeated units of the crystal are arranged. A crystal lattice can therefore be described by its underlying Bravais lattice and the arrangement of atoms, ions or molecules within a particular unit cell, i.e. the basis [2]. This principle is used in a number of ways during this study. Firstly, this process is performed on a finite scale to construct a 64 atom supercell of CZTS from the 8 atom primitive unit cell for use in density functional theory (DFT) calculations to predict defect formation energy. This process is discussed further in section 3.1.2. The principle is also used in all DFT calculations of solid state systems through the implementation of periodic boundary conditions to simulate an infinite, bulk system using only a finite unit cell.

Another important concept in the theoretical modelling of periodic structures is reciprocal space

and the reciprocal lattice. Converting to reciprocal space enables the description of periodic features with a longer-range periodicity than the unit cell in real space, such as the motion of electrons in a crystal and phonons. In the same way that any quantity that varies with time can be described as a sum of Fourier components in the frequency domain; the spatial properties of a crystal can be described as a sum of components in Fourier space, otherwise known as reciprocal space or  $k$ -space. The reciprocal lattice of a perfect single crystal is an infinite periodic 3D array of points whose spacings are inversely proportional to the distances between the planes in the lattice in real space. Vectors in real space have dimensions of length, whereas vectors in reciprocal space have dimensions of length $^{-1}$ . This can therefore be compared directly to the wavevector ( $k = \frac{2\pi}{\lambda}$ ) of an excitation such as a phonon or a moving electron and multiplication of each coordinate of the reciprocal lattice by  $\hbar$  converts reciprocal space into momentum space as for a quantised wave  $\mathbf{p} = \hbar\mathbf{k}$  [12].

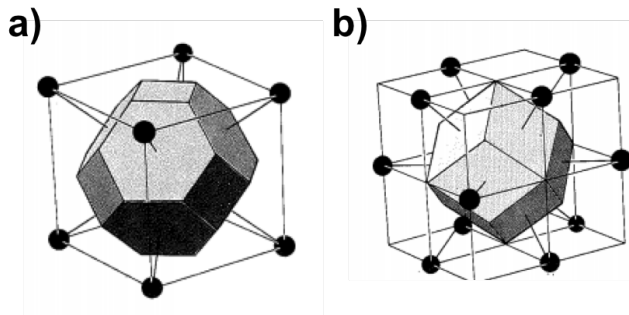


Figure 2.1: The Wigner-Seitz cell for the body-centred cubic Bravais lattice where there is a lattice point at its centre and on each vertex. The hexagonal faces bisect the lines joining the central point to the points on the vertices. The square faces bisect the lines joining the central point to the central points in each of the six neighbouring cubic cells. Figure taken from reference 2.

The Wigner-Seitz primitive cell is the most common choice of primitive cell with the full symmetry of the Bravais lattice. It represents the region of space around a lattice point that is closer to that point than to any other lattice point. For example, figure 2.1a shows the truncated octahedron that is the Wigner-Seitz cell for a body-centred cubic (bcc) lattice [2]. The first Brillouin zone is the Wigner-Seitz primitive cell of the reciprocal lattice. The reciprocal of the bcc lattice is face-centred cubic (fcc), therefore the first Brillouin zone of the bcc lattice is the fcc Wigner-Seitz primitive cell as shown in figure 2.1b [3]. As the full symmetry of the

reciprocal lattice is contained within the first Brillouin zone, it is only necessary to sample  $k$ -points within this single unit cell of the reciprocal lattice when calculating the electronic ground state of a periodic structure.

## 2.2 Band Theory & Band Structure of Semiconductors

Refer to: pg 18 [149], pg 105 112 128 131 137 [14], pg 111 + 119 [51]

The band theory of solids provides a means to explain the difference in the electrical conductivity of conductors, semiconductors and insulators. Electrons bound to an atom have a number of possible discrete energy levels. When a large number of atoms are brought together to form a solid, it becomes impossible to assign individual electrons to individual atoms. Instead, the electrons are considered to be shared amongst the atomic nuclei. However, a consequence of this sharing would be a large number of electrons occupying the same energy state, which violates the Pauli Exclusion Principle. The original discrete energy levels therefore are broadened into bands. The new energy levels are so closely spaced that they are considered to be a quasi-continuous band of allowed energies. This is illustrated in figure 2.2. The series of bands of allowed energies in a semiconductor or insulator are separated by bands of forbidden energy, known as the band gap,  $E_g$ , of the material [151]. In the simplest model, the upper energy band (the conduction band) is separated from the lower energy band (the valence band) by a constant band gap. This is called the flat band model. In real structures, the band architecture is more complicated than this simple model [129].

The concept of the energy band model of a solid emerges from considering the behaviour of electrons in a periodic crystal lattice, but cannot be understood in terms of classical physics alone. Instead, the electron must be considered in terms of wave-mechanical terms as a wave propagating in a periodic structure with diffraction and interference effects [70]. In the band theory of solids, the energy of a single electron in a perfect crystal is described by the one-

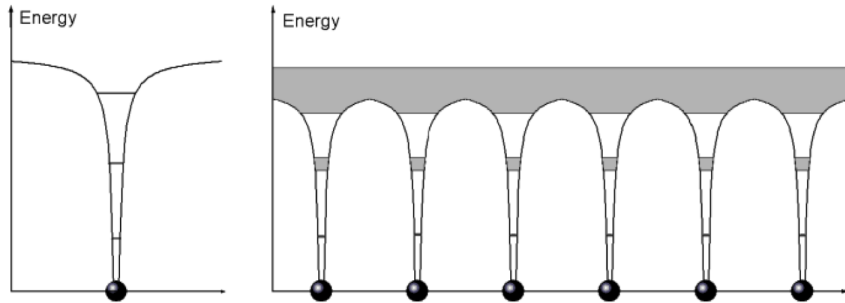


Figure 2.2: Electron energy levels of a single atom (left) and the formation of a quasi-continuous band of allowed energies in a solid crystal when many atoms are brought close together (right). Figure taken from 102.

electron Schrödinger equation, shown in equation 2.1. The first term in equation 2.1 is the kinetic energy of the electron,  $V(\mathbf{r})$  is the effective non-zero periodic potential energy experienced by the electron in the crystal,  $\psi$  is the electron wavefunction and  $\epsilon$  is the eigenenergy of the electron. In band theory, it is assumed that for any electron, everything else in the crystal can be represented by the effective potential energy,  $V(\mathbf{r})$  [13].

$$\left[ \left( -\frac{\hbar^2}{2m} \right) \nabla^2 + V(\mathbf{r}) \right] \psi = \epsilon \psi \quad (2.1)$$

The spatial dependence of the potential experienced by an outer electron in a crystal for multi-electron systems was considered by Felix Bloch. He determined that the total potential is the sum of two parts. Firstly, the electrostatic potential due to the array of atomic cores. For a perfect lattice this should have the translational periodicity of the lattice. Secondly, the potential due to all other electrons. Bloch assumed that the charge density would have the same long-term average value in every unit cell of the crystal and therefore would be periodic. Bloch's theorem states that the wavefunction which satisfies equation 2.1 subject to a periodic potential should be of the form shown in equation 2.2, where  $U_k(\mathbf{r})$  is some function (depending on the value of the wavevector,  $\mathbf{k}$ ) that also has the complete periodicity of the lattice and  $\mathbf{k}$  is confined to the first Brillouin zone [13].

$$\phi_k(\mathbf{r}) = U_k(\mathbf{r}) e^{i\mathbf{k}\cdot\mathbf{r}} \quad (2.2)$$

$$\psi_k(\mathbf{r}) = \sum_k A_k \phi_k(\mathbf{r}) = \sum_k A_k U_k(\mathbf{r}) e^{i\mathbf{k}\cdot\mathbf{r}} \quad (2.3)$$

Due to the translational symmetry of a crystal lattice, an eigenfunction of the one-electron Schrödinger equation can be expressed as a sum of Bloch functions such as that shown in equation 2.2, as shown in equation 2.3. The one-electron wavefunctions therefore can be indexed by constants  $\mathbf{k}$ , which are the wave vectors of the plane waves forming the ‘backbone’ of the Bloch function. A plot of the electron eigenenergies from equation 2.1 versus  $\mathbf{k}$  is known as the electronic band structure of the crystal [149].

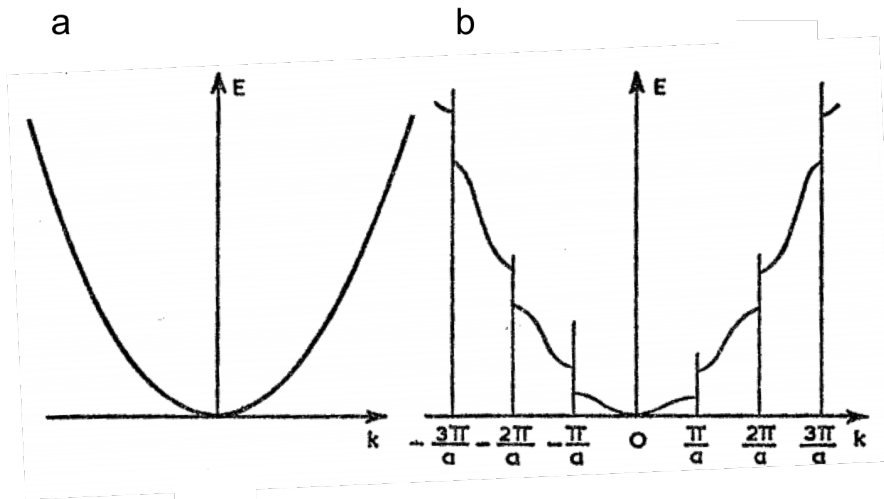


Figure 2.3: Energy-wave vector diagrams: (a) the free electron parabola, (b) modification due to a periodic crystal lattice. Figure taken from reference 70.

The introduction of a medium with a discrete structure, such as a crystal lattice, has a profound effect on the dispersion relation of the waves. The energy dispersion relation of a free electron and that in a periodic crystal lattice is shown in figure 2.3. A periodic medium does not completely suppress the propagation of waves, as would be expected in disordered or amorphous structures, but they do however introduce limiting frequencies and wavelengths for the propagation, followed by cut-off regions. The lower limit of the wavelength is set by the lattice spacing,  $a$ , giving an upper limit of the wave vector,  $\mathbf{k}$ , of  $\frac{\pi}{a}$ . As figure 2.3 shows, the parabola of the free electron is modified in a periodic crystal by the introduction of discontinuities at values of  $\mathbf{k}$  corresponding to multiples of  $\frac{\pi}{a}$ . The appearance of such energy gaps implies that electrons in a periodic crystal may only have kinetic energies corresponding to certain bands,

whilst being free to propagate in the lattice [71].

Each electron occupies a state of definite  $\mathbf{k}$ . Therefore, an infinite number of electrons within the solid would result in an infinite number of  $k$ -points. At each  $k$ -point, only a finite number of the available energy levels will be occupied. Therefore only a finite number of electrons need to be considered but at an infinite number of  $k$ -points. In practise, all of these  $k$ -points are not considered. Electron wavefunctions will be almost identical for values of  $\mathbf{k}$  that are sufficiently close, so the wavefunctions over a region of reciprocal space can be represented by considering the wavefunction at a single  $k$ -point. It is therefore sufficient to consider the electronic states at a finite number of  $k$ -points in order to determine the ground state energy of the solid. This approximation is illustrated in figure 2.4. Using Bloch's Theorem therefore has enabled the ground state energy to be determined by considering only the number of electrons in the unit cell at a finite number of  $k$ -points, which are chosen to sample the Brillouin zone appropriately. The choice here is a balance between more  $k$ -points for a more accurate representation of the Brillouin zone and fewer  $k$ -points to reduce the computational expense of the calculation [131].

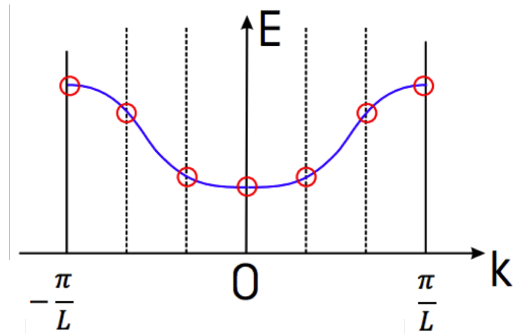


Figure 2.4: The energy dispersion relation for electrons moving in a crystal, illustrating how the function can be approximately represented by a finite number of  $k$ -points, which form an equally-spaced mesh. Figure adapted from reference 36.

The energy band model has been successful in explaining many aspects of the behaviour of solids and a large amount of experimental data collected has supported the theoretical predictions made using the model. Its main drawback however is that it assumes a perfect, or nearly perfect, crystal lattice. It applies well to single crystals and polycrystalline substances, but

cannot be applied to materials that are amorphous or heavily disordered so that the structure deviates significantly from the periodicity of the crystal [70]. Low concentrations of impurities and defects can be modelled by considering, for example, the introduction of additional donor and acceptor energy levels within the band gap of a material and the scattering of electrons and holes in the solid. However, at higher defect concentrations the band profile can be modified as shown in figure 2.5 to give rise to conductivity even at temperatures that are too low to produce excitation of carriers into the free conduction bands, called impurity band conduction [71].

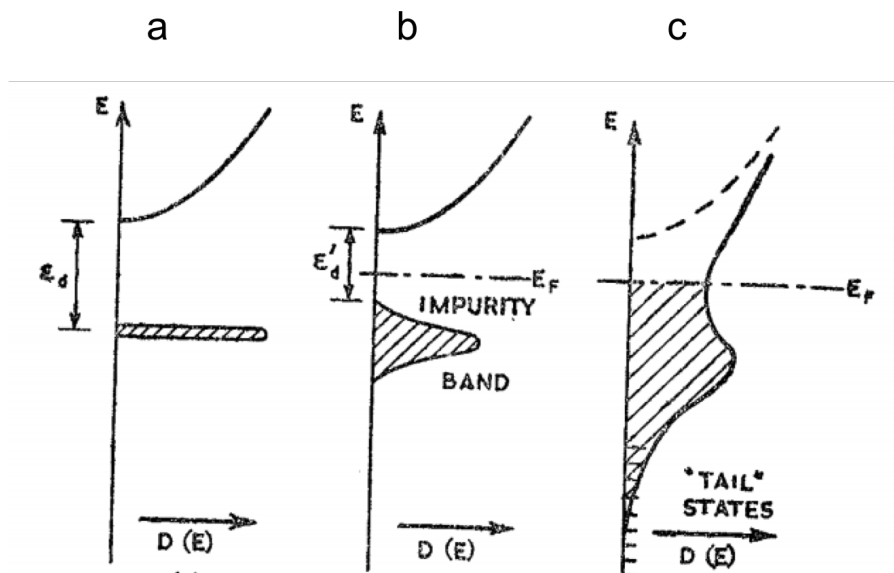


Figure 2.5: The influence of increased donor impurity density on the conduction band profile showing low (a), medium (b) and high (c) densities of impurities. Figure taken from reference 71.

A useful concept used to simplify the dynamics of an electron in a crystal lattice in the band theory of solids is that of effective mass, which was first mentioned in section 1.1.3 as a key material property for a solar absorber material. The effective mass is a convenient parameter which accounts for the influence of a periodic lattice on a free carrier, enabling an electron in a periodic crystal to be treated as though it were a free particle but with a different mass in calculations of charge transport. Values of effective mass in semiconductors usually vary between 0.01 and 1 times the mass of a free electron and it is determined by the curvature of the energy graph in  $k$ -vector space [71]. The effective mass is a parameter that can influence the efficiency of a solar cell, in particular, the effective mass of holes in the valence band and

electrons in the conduction band (i.e. minority charge carriers) are of interest. The mobility of charge carriers is inversely proportional to the effective mass and the mobility of charge carriers in a PV material is important for efficient charge collection [6].

## 2.3 Crystal Imperfections & Disorder

Refer to: pg 160 [149], pg 51, 52, 64 [14], pg 63 + 65 [51]

- Notes from A. Guinier 'X-Ray Diffraction' CH6 + Ziman
- Mention many types of disorder possible for multicomponent, especially for multi-component, compound semiconductor. e.g. of many types of possible defects for CdTe from Ken's work - and that's just binary!
- Extended defects usually detectable?
- Discuss frozen in disorder and Scragg's work?

## 2.4 Solar Cell Performance Bottlenecks Due to Crystal Imperfections

Refer to: pg 217 221 [14]

Impact of Defects and Disorder on Photovoltaic Performance:

- SRH recomb, GBs, secondary phases, band gap and electrostatic potential fluctuations
- See CMP lectures on defects + ebook reading material

Band Tailing in Disordered Semiconductors:

- See culprit section 6.1 on Urbach tails
- Metal disorder in CZTS due to limited cooling/ annealing times, link to Jonathan Scragg's work (years to cool to perfect crystal)
- Nelson, pg 65, 3.5.4: heavy doping leading to band tailing
- see Pankove + Russian 1970s papers, Urbach tail, fluctuations in electrostatic potential
- See Urbach tail doc (pg 36) and use Cu/ Zn culprit paper + link to eris
- See desktop papers from Jarv x2

## 2.5 Characterization of Defects

\*\*See defect tutorial paper\*\*

### 2.5.1 First-Principles Calculations

### 2.5.2 Emission Spectroscopies of Semiconductors

Refer to: pg 10 [15], pg 345 [149]

- See above books + old transfer report
- Cardona, S7.1 Emission Spectroscopies
- Photoluminescence (PL) imaging is becoming a popular method to inspect solar cell materials, it does not require a full functioning device and can be a powerful tool for

probing defects in semiconductors [? ? ]. The PL spectra of  $\text{Cu}_2\text{ZnSnS}_4$ (CZTS) provides clear evidence of disorder in the material.

- Overview of technique, information gained from technique, T dependent PL, PL spectra of CZTS: single crystal and thin film.

Photoluminescence (PL) spectroscopy is an example of a spatially resolved characterization technique, which can be used to give spatial information on the inhomogeneities in a PV device that cause a reduction in expected performance parameters, such as the  $V_{OC}$ . PL is an imaging technique involving a one-step acquisition of the local properties of a whole PV device using an imaging device, compared to the typically lengthy step-by-step procedures required in scanning techniques, such as electron beam induced current (EBIC) and light beam induced current (LBIC). Luminescence imaging techniques involve using an imaging device to capture the photons emitted by radiative recombinations following the excitation of charge carriers in PV devices. In the case of PL, light is used for the excitation whereas in electroluminescence (EL) charge carriers are electrically excited. For an EL measurement therefore, the PV material must have electrical contacts. PL however is a contactless method and so firstly neglects the effects of the contacts on the conversion efficiency distribution but secondly can be carried out during earlier stages of the manufacturing, i.e. before the electrical contacts have been made [15].

### 2.5.3 Photoluminescence Spectra of $\text{Cu}_2\text{ZnSnS}_4$

See word doc overview

PL is a particularly common characterisation technique used on CZTS with several such studies having been performed already. References 43, 48, 52, 78, 109 are just some examples of such studies. Low temperature PL specifically is a powerful tool for probing defects in semiconductors [42] and ...

Notes from Pankove, notes from JC talk, figure showing common PL recombination mechanisms.

PL measurements have been performed on both polycrystalline CZTS [109, 87, 132] and single crystals of CZTS [52, 80, 55]. Polycrystalline samples are more similar to those likely to be used in thin-film CZTS photovoltaic devices, however comparison between those measurements with single crystal measurements could enable the isolation of recombination at grain boundaries from those due to bulk defects and secondary phases present within a single grain... relate to earlier section on polycrystalline thin-film PV

However, there is some disagreement in the literature about the main recombination mechanisms that could explain the observed PL spectra.

(mention two models of QDAP and elec pot fluc, Eg and charged defect induced + relate to Cu-Zn disorder)

#### **2.5.4 Modulation Spectroscopy & Band Gap Broadening**

See pdf from Laurie - method used by PVTEAM to measure band gap broadening of CZTS single crystal + see quantum processes in semiconductors pg 244

### **2.6 Novel Optoelectronic Phenomena for High Performance Solar Cells**

#### **2.6.1 Spin Orbit Interaction & Rashba Splitting**

Refer to: pg 13 + 21-22 [8] + quantum processes in semiconductors pg 13 for SOC

see webpages: pg 84 for discussion of effect of SOC on lattice without inversion symmetry! + useful slide

Look for textbook source?

See rashba splitting paper (pre-Duke visit papers)

## 2.6.2 Photovoltaic-Ferroelectric Phenomena

Ferroelectric PV materials are currently receiving a great deal of research interest, however the origin of their PV properties are considered to be unresolved [146]. A large number of theories have been proposed in an attempt to explain the two observed ferroelectric-photovoltaic (FE-PV) phenomena: the bulk PV effect (BPE), also referred to as the photogalvanic effect, and the anomalous PV effect (APE). In the BPE, a direct current appears in a homogeneous medium under uniform illumination and this can occur in all materials without a center of symmetry [9]. Ferroelectric materials exhibit this effect strongly [146] and the first observation of this effect was in 1956 with photovoltages measured in un-doped single crystals of the ferroelectric material BaTiO<sub>3</sub> [29]. In the case of the APE, photovoltages have been measured that are orders of magnitude larger than the band gap of the material [125], but has been observed to disappear when the sample undergoes a phase transition to a paraelectric phase [105], and so no longer exhibits spontaneous electric polarization. Theories have been developed to explain the FE-PV phenomena based around experimental observations of factors that have been shown to influence the photovoltage of FE-PV devices, such as: the distance between the two opposite electrodes [59, 107], intensity of incident light [20], electrical conductivity [39], remnant polarization of the ferroelectric crystals [21], crystallographic orientation [58], the dimension or size of the crystals [107, 60], domain walls [145] and the interface between the FE material and the electrode [67].

Models have been proposed to explain the BPE in ferroelectric materials based upon the built-in asymmetry of non-centrosymmetric crystals. One model is based on asymmetric scattering

centres in the materials [9]. In non-centrosymmetric crystals, the rate of the generation of charge carriers with momenta  $\pm k$  can be different due to asymmetric electron-hole scattering. A ‘ballistic current’ can then be generated due to the momentum imbalance [74]. Another model, the shift current model [74], has been proposed, which is based on the asymmetry of the electron density [23]. Light-induced transitions of charge carriers between bands in reciprocal space are accompanied by asymmetrical shifts in real space between atoms in elementary cells [74]. Such currents have been demonstrated for a number of materials, such as GaAs [123] and BiFeO<sub>3</sub>, where this has been demonstrated using both computational [147] and experimental [68] techniques.

The domain wall theory has been proposed to explain the large generated photovoltages in the APE [10] and the Schottky-junction effect [153] and depolarization field model [22, 126], also referred to as the screening effect, have been proposed as additional contributions to the large photovoltage. Unlike the BPE, some theories to explain the APE rely on the nano- and microstructure of the material [23]. The latter two theories are related to the interface between the FE material and an electrode in a FE-PV device, but were originally neglected as the contributions to the photovoltage were believed to be small. However, these effects become more significant in thin-film devices where photovoltages are typically low [150], and thin-films are particularly relevant for PV applications.

The domain wall theory was developed to explain observations of photovoltages in thin films of BiFeO<sub>3</sub> increasing linearly with the total number of ferroelectric domain walls along the net direction of electric polarization and vanishing along the direction perpendicular to the net polarization [145]. In this theory, the narrow ferroelectric domain walls drive the dissociation of photogenerated excitons and so act as nanoscale photovoltage generators connected in series. The photocurrent across the domain walls is therefore continuous but the photogenerated voltage accumulates along the direction of net polarization, allowing for photovoltages that are considerably larger than the band gap of the material [150]. In the Schottky-junction effect, the FE semiconductor forms a Schottky contact with the metal electrodes, which then generate

a photocurrent under illumination due to the local electric field caused by the band bending near to the electrode. This photocurrent is dependent upon the Schottky barrier height and depletion region depth, but the photovoltage is still limited to the band gap of the material. Further, the additional photovoltage contribution from this effect can be cancelled out if the same electrode contacts are used, due to the opposite polarization of the two Schottky-junctions [150]. In the depolarization field model, high densities of polarization charges are believed to accumulate on surfaces of polarized FE films, this then induces a large electric field inside the FE layer if the charge is not screened. This effect will be far more pronounced in a thin-film device. The electric field is thought to not be fully screened by the free charges in the metal or semiconductor that the FE layer is in contact with, resulting in a depolarization field. This depolarization field will be larger when the FE material has a large remnant electric polarization, the FE layer is thinner and when it is in contact with a semiconductor, as opposed to a metal, due to fewer free charge carriers and higher dielectric constant in a semiconductor than a metal, giving weaker screening. The depolarization field is believed to be the dominating force for the separation of photogenerated charge carrier pairs [150].

Clearly the exact mechanism behind the observed PV phenomena in FE materials are not yet fully understood, but they could open up new possible routes for materials to enable higher performance solar cells. In particular, the APE could be utilized for materials with higher  $V_{OC}$  to enable a higher power output from a solar cell. Additionally, it has been suggested that ferroelectric domains may be able to drive the separation of photoexcited electron-hole pairs to reduce detrimental recombination in solar absorber materials [40].

# Chapter 3

## Methodology

### 3.1 Calculation of the Formation Energy of Defects in Cu<sub>2</sub>ZnSnS<sub>4</sub>

See Lany paper + Keith's posted paper + encyclopoedia of defects paper

As discussed in section 2.4, defects in a solar absorber material can heavily impact on the performance of a photovoltaic device composed of that material. In this study we perform first principles calculations of two types of defects in the solar absorber material Cu<sub>2</sub>ZnSnS<sub>4</sub>. We firstly performed calculations of the formation energy of the charge neutral Cu-on-Zn and Zn-on-Cu anti-site defect pair, [Cu<sub>Zn</sub><sup>-</sup> + Zn<sub>Cu</sub><sup>+</sup>], in order to parameterize our Monte Carlo simulations of thermodynamic Cu-Zn disorder, which is discussed further in section 3.2. We also begin calculations of the formation energy of a sulfur vacancy in Cu<sub>2</sub>ZnSnS<sub>4</sub>. This defect can however take on three different charge states: V<sub>S</sub><sup>0</sup>, V<sub>S</sub><sup>+1</sup> and V<sub>S</sub><sup>+2</sup>, where electron occupancy varies from two to one to none respectively. We will then go on to calculate the formation energy as a function of the sulfur chemical potential to determine which charge state has the minimum formation energy at typical annealing conditions of Cu<sub>2</sub>ZnSnS<sub>4</sub>, in terms of temperature and pressure. This methodology is outlined in section 3.1.3. However, special correction techniques

must be applied when performing periodic calculations to simulate a bulk system with a finite unit cell when the unit cell possesses a net charge. This point is discussed in section 3.1.2.

### 3.1.1 Density Functional Theory & Hybrid Functionals

See Bechstedt book [8] + figures from Aron + discuss band gap underestimation in standard DFT (GGA mentioned during intro, also discuss GGA+U and limitations)

The description of the electrons in a system requires the use of QM... outline of standard DFT... situations in which standard DFT fails and why we need to use hybrid-DFT.

### 3.1.2 The Supercell Method & Corrections for Charged Defects

see Aron's lectures + DFT in materials science paper [90]

### 3.1.3 Defect Formation Energy & Equilibrium Concentration

Show formula for defect formation E as a function of electronic and atomic chemical potentials, discuss chemical potentials (especially S!) and show Boltzmann expression for concentration.

## 3.2 Monte Carlo Simulation of Thermodynamic Disorder in Cu<sub>2</sub>ZnSnS<sub>4</sub>

### 3.2.1 Mapping the Crystal Structure of Cu<sub>2</sub>ZnSnS<sub>4</sub> onto a Simple Lattice

In this study, we use a custom Monte Carlo code to simulate substitutional on-lattice disorder between Cu and Zn ions in Cu<sub>2</sub>ZnSnS<sub>4</sub> as a function of temperature. The crystal structure of

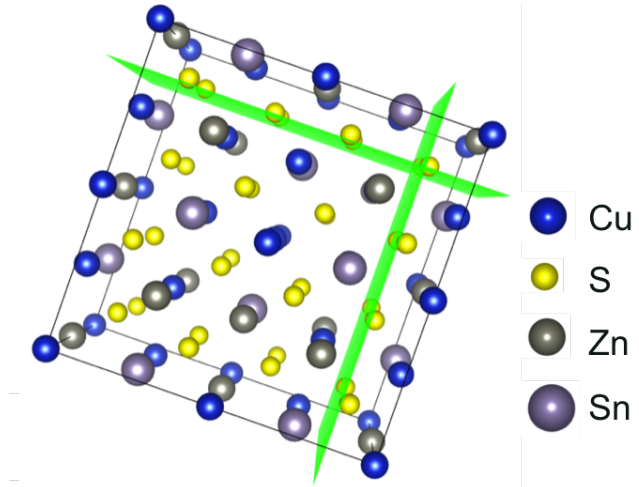


Figure 3.1: A supercell of the perfect Cu<sub>2</sub>ZnSnS<sub>4</sub> crystal lattice, which can be described by inter-penetrating face-centred cubic sub-lattices: one of metal cations and one of sulfur anions. Green planes are used as guides to the eye to show planes of S anions that form one of the two face-centred cubic sub-lattices.

Cu<sub>2</sub>ZnSnS<sub>4</sub> can be described by two inter-penetrating face-centred cubic (FCC) lattices: one of metal cations and one of sulfur anions, as shown in figure 3.1. We consider the sulfur sub-lattice to be stationary because any substitution between ions in the cation sub-lattice and sulfur anion sub-lattice would be energetically infeasible and any substitutions amongst the sulfur anions in that sub-lattice would be energetically equivalent. The sulfur sub-lattice is therefore neglected during the Monte Carlo simulations but incorporated later in calculations of lattice electrostatics. This then reduces the problem of mapping the Cu<sub>2</sub>ZnSnS<sub>4</sub> crystal structure onto a simple lattice to just one FCC cation lattice. We then map this onto a simple cubic (SC) lattice for our simulations by introducing empty lattice sites into the SC lattice. The crystal structure of Cu<sub>2</sub>ZnSnS<sub>4</sub> can also be described by alternating layers of Cu-Zn and Cu-Sn [112], as shown in figure 1.11. We therefore fill the lattice in this way in a checkerboard-like fashion when constructing a perfectly ordered on-lattice representation of the crystal structure, 2D slices of the ordered system are shown in figure 3.2. During our simulation the separation between lattice sites is one lattice unit but this is re-scaled for calculations of lattice electrostatics using our DFT-optimised lattice parameters of  $\frac{a}{2} = \frac{b}{2} = \frac{5.44}{2} \text{\AA}$ . Where the lattice parameters are divided by 2 as empty sites are placed in between ions to map the FCC structure onto an SC lattice. Figure 3.3 shows flat representations of the crystal structure, with empty lattice sites marked out by crosses. Lattice parameter c for our model will then be approximated to 2a,

which is very close to the DFT-optimised value of 10.86 Å.

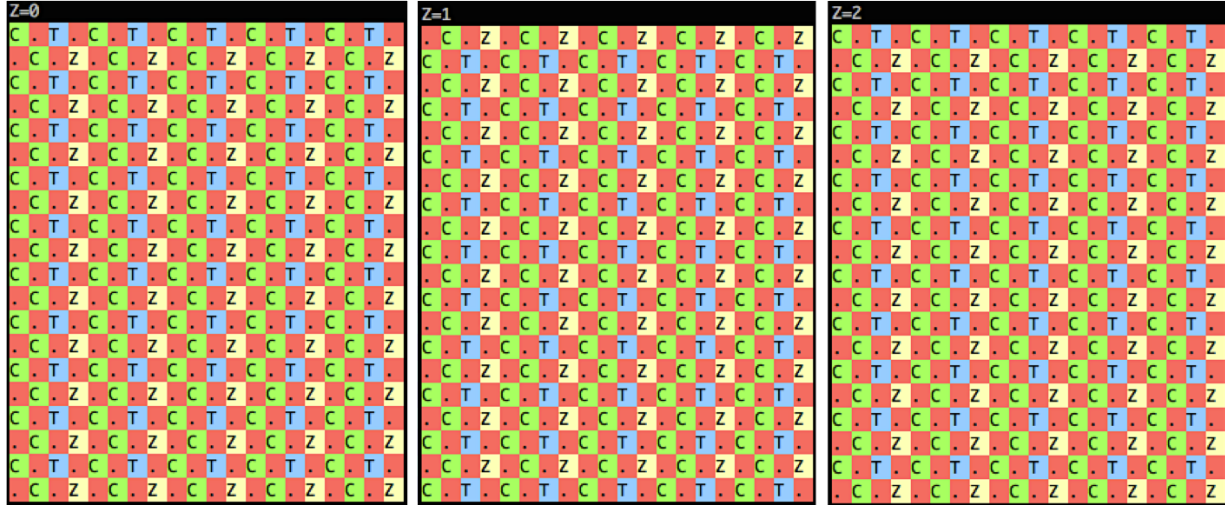


Figure 3.2: A two-dimensional (x-y) slice of a 20x20x20 cation sub-lattice of ordered  $\text{Cu}_2\text{ZnSnS}_4$ . Sulfur anions are neglected from the simulations and the face-centred cubic cation lattice is mapped onto a simple cubic lattice by including empty sites in the lattice. Alternating layers in the z-direction are displaced by one lattice unit in order to reproduce the correct kesterite structure. ‘C’, ‘Z’, ‘T’ and ‘.’ represent copper, zinc, tin and an empty site respectively.

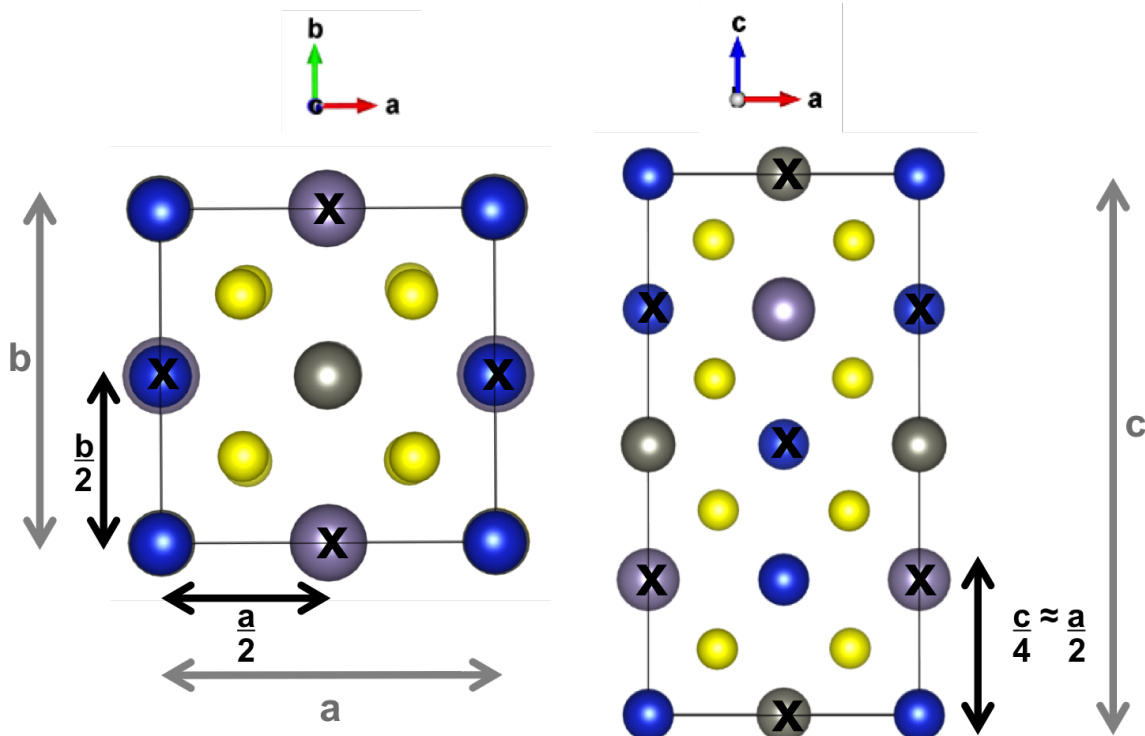


Figure 3.3: Flat visuals of the  $\text{Cu}_2\text{ZnSnS}_4$  crystal structure showing positions of empty sites (denoted by x's) used to map the face-centred cubic lattice of the cations onto a simple cubic lattice. Lattice parameters obtained from hybrid density functional theory geometry optimizations are  $a = b = 5.43770 \text{ \AA}$  and  $c = 10.85670 \text{ \AA}$ , and so  $c$  is approximately  $2a$ .

### 3.2.2 Monte Carlo Simulation with the Metropolis Algorithm

The Monte Carlo method can be used to calculate thermodynamic information about a system of N interacting ions represented on a 3D lattice by using classical statistics, considering only two-body forces and assuming that the potential field of an ion is spherically symmetric. If we know the positions of the N interacting ions on the lattice then the potential energy of the system can be calculated using equation 3.1, where V is the Coulombic potential between two ions and  $d_{ij}$  is the minimum distance between ions i and j [86].

$$E = \frac{1}{2} \sum_{i=1}^N \sum_{j=1}^N V d_{ij} \quad (3.1)$$

To calculate the properties of the system, the canonical ensemble is used where the temperature, number of ions and volume are all constant. In this ensemble, the equilibrium value for any quantity of interest, B, is given by equation 3.2, where  $E_\alpha$  is the energy of the system when in state  $\alpha$  and  $p_\alpha$  is the probability of the system being in state  $\alpha$ .

$$\langle B \rangle = \frac{\sum_\alpha e^{-\frac{E_\alpha}{k_b T}} B_\alpha}{\sum_\alpha e^{-\frac{E_\alpha}{k_b T}}} = \frac{\sum_\alpha e^{-\frac{E_\alpha}{k_b T}} B_\alpha}{Q} = \sum_\alpha B_\alpha p_\alpha \quad (3.2)$$

$$p_\alpha = \frac{e^{-\frac{E_\alpha}{k_b T}}}{\sum_\alpha e^{-\frac{E_\alpha}{k_b T}}} = \frac{e^{-\frac{E_\alpha}{k_b T}}}{Q} \quad (3.3)$$

$Q$  in equation 3.2 is called the partition function. For most systems calculating the value of the partition function requires the summation over a large number of states. When applying the Monte Carlo method to a system of particles, the summation over discrete states for  $Q$  is replaced by a set of integrals. This is shown in equation 3.4 where  $U(\mathbf{r}^N)$  is the potential energy of the system which depends upon the position,  $\mathbf{r}$ , of the N interacting ions in the system and  $Z_{NVT}$  is the configurational integral [79].

$$\langle U \rangle = \frac{\int e^{-\frac{U(\mathbf{r}^N)}{k_b T}} U(\mathbf{r}^N) d\mathbf{r}^N}{\int e^{-\frac{U(\mathbf{r}^N)}{k_b T}} d\mathbf{r}^N} = \frac{\int e^{-\frac{U(\mathbf{r}^N)}{k_b T}} U(\mathbf{r}^N) d\mathbf{r}^N}{Z_{NVT}} \quad (3.4)$$

The configurational integral is over the three coordinates of each ion, as shown in equation 3.2.2. There are therefore  $3N$  coordinates that define all possible configurations of the system.

$$d\mathbf{r}^N = dx_1 dy_1 dz_1 dx_2 dy_2 dz_2 \dots dx_N dy_N dz_N \quad (3.5)$$

For a system containing several hundred ions this would be a several-hundred dimensional integral over the configuration space, which would be impractical to carry out by the usual numerical methods. The Monte Carlo method for many-dimensional integrals is used for this purpose [86]. It is conceptually easiest to think about this method for a one-dimensional integral. This method involves sampling a large number of random points within a region defined by the limits of the integral. The integrated function is then the fraction of points that fall below the curve of the function multiplied by the area of the sampled region. The value obtained becomes a better approximation to the actual value of the integral as the number of random numbers, called Monte Carlo steps (MCS), used to sample the integration region increases. [79].

The Standard Monte Carlo method for our system would involve placing each of the  $N$  ions at random positions in the lattice to define a random point in the  $3N$ -dimensional configuration space. The energy of the system would then be calculated using equation 3.1 and the configuration would then be weighted using  $e^{-\frac{U(\mathbf{r}^N)}{k_b T}}$  when obtaining the equilibrium value of  $U$ . However, many configurations are very improbable so performing this calculation for every possible configuration would be inefficient and unnecessary to sufficiently evaluate the ensemble. The custom Monte Carlo code in this study makes use of the Metropolis modified Monte Carlo scheme [86]. In this implementation of the Monte Carlo method, instead of choosing configurations randomly and then weighting them, the Metropolis algorithm considers the relative probability of a system being in a new configuration,  $\beta$ , to that of being in the current configuration,  $\alpha$ . This is shown in equation 3.6, where  $E_\alpha$  is the energy of state  $\alpha$  and  $E_\beta$  is the energy of state  $\beta$ .

$$\frac{p_\beta}{p_\alpha} = \frac{e^{-\frac{E_\alpha}{k_b T}}}{Q} \frac{Q}{e^{-\frac{E_\alpha}{k_b T}}} = e^{-\frac{E_\beta - E_\alpha}{k_B T}} \quad (3.6)$$

The relative probabilities of the two states are completely determined by the energy difference,

such that if:

$$\Delta E = E_\beta - E_\alpha \leq 0 \text{ then } \frac{p_\beta}{p_\alpha} \geq 1 \quad (3.7)$$

and if

$$\Delta E = E_\beta - E_\alpha > 0 \text{ then } \frac{p_\beta}{p_\alpha} < 1 \quad (3.8)$$

The Metropolis algorithm creates a list of configurations through configuration space that has the correct probability distribution. This list is called a trajectory through configuration space. The approach involves making a trial move of the system to a new configuration, in the case of our study this would be a substitution between a Cu and a Zn ion. It is then decided if this new configuration should be added to the trajectory or not based on the probability of the new configuration relative to the current configuration. If the relative probability is  $\geq 1$ , as shown in equation 3.7, then the move is accepted and added to the trajectory. However, if the relative probability is  $< 1$  then the move will only be accepted if  $e^{-\frac{\Delta E}{k_B T}} \geq$  a random number generated between 0 and 1 [79].

### 3.2.3 Equilibration & Finite Size Effects

Our Monte Carlo model for Cu-Zn disorder is analogous to the Ising model of a magnet, descriptions of which can be found in many textbooks such as references 91 and 75. In the case of an Ising model, the trial moves in the Metropolis algorithm are spin flips, whereas in our model the trial moves are swaps between Cu and Zn ions. In the case of the Ising model it is usually the average magnetization of the system or internal energy as a function of temperature that are the quantities of interest. In our system, it is the distribution of the electrostatic potential across the system that is of interest, as this can be related to the observed band tailing. We are also interested in the corresponding configuration of the ions (and extent of disorder) that results in such a distribution. In the case of the Ising model when, for example, determining the magnetization of a system at a given temperature, the simulation must be run for a suitably long time until the system has come to equilibrium at that temperature. This is referred to as the equilibration time and the point at which a system has attained equilibrium

can be defined as being when the average probability of finding the system in any particular state  $\alpha$  is proportional to the Boltzmann weight of that state,  $e^{-\frac{E_\alpha}{k_b T}}$ . Once the system has equilibrated, the quantity of interest such as the magnetization must then be again measured over a suitably long time and averaged [91].

To gauge if a system has reached equilibrium, in the case of the Ising model, it is common practice to run the simulation for a large number of Monte Carlo steps (MCS) (where one MCS corresponds to attempting a trial spin-flip at all sites in the system once) and looking for how the value of a quantity of interest, such as the average magnetization across the system, changes with increasing number of MCS as the simulation progresses. Equilibration is often considered as the point at which the value of a quantity of interest, which initially changes by a large amount, eventually converges to fluctuating about a steady average value. An example of this is shown in figure 3.4a. This is dependent upon the principle that a system in equilibrium spends the overwhelming majority of its time in a small subset of states in which its properties take a narrow range of values [91]. In the case of our system, it is the distribution in electrostatic potential across the system that is of interest so we will look for a point after which the variance of the distribution of electrostatic potentials across the system has reached a steady value.

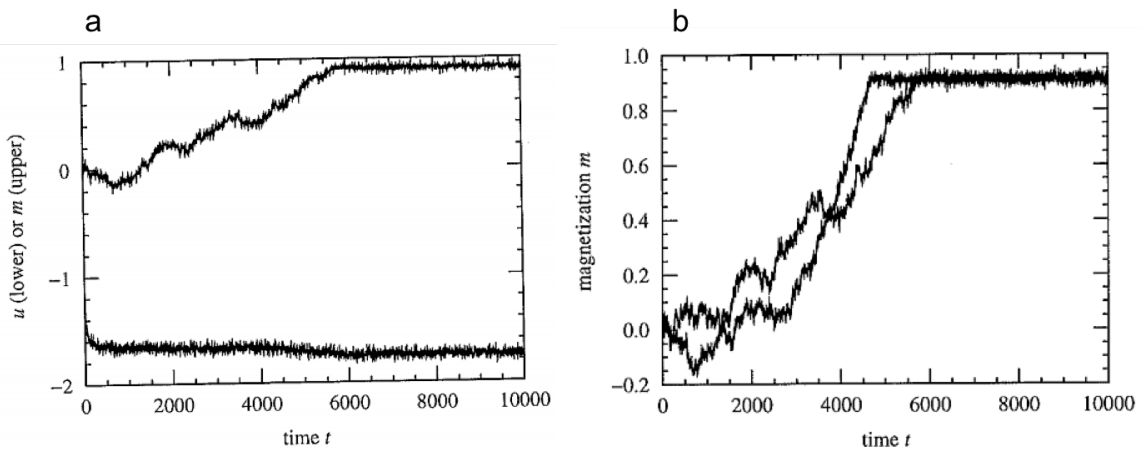


Figure 3.4: The magnetization (upper curve) and internal energy (lower curve) per site of a two-dimensional Ising model simulated using the Metropolis algorithm (a). Magnetization as a function of time for two different simulations (b). Time is measured in Monte Carlo steps per lattice site. Figures taken from 91.

Provided the simulation is allowed to run for a sufficiently long time to reach this minimum configuration, the final configuration for a given system at a given temperature should always

be the same, this point is illustrated in figure 3.4b. However, as this is a stochastic method, making use of sampling many times with random numbers in order to determine the minimum energy configuration of the system, the trajectory to reach this final configuration will by nature be random and so we can draw no conclusions from configurations of the system until the final configuration at the particular temperature is reached. Even then we must consider the possibility of our system finding local minima instead of global minima, and therefore giving a false impression of having equilibrated. For this reason we perform multiple runs of the simulations, each seeded with different random numbers to ensure that the same final configurations, and associated equilibrium properties, are obtained.

As simulations are performed for finite lattices, in order to simulate a bulk system the edges or ‘boundaries’ of the system must be treated carefully. The boundaries can be effectively eliminated through the use of periodic boundary conditions (PBCs). In the case of an Ising model, this means that the first spin in a row interacts with the last spin in the row as if it were a nearest neighbour, and vice versa [75]. This principle is illustrated in figure 3.5. Although this procedure effectively eliminates boundary effects, the system is still characterized by the finite lattice size,  $L$ , which limits the correlation length to  $\frac{L}{2}$ . Resultant properties of the system may then differ for the bulk system than for the simulated system. We therefore perform simulations with increasing system size to look for any differences in the quantities of interest.

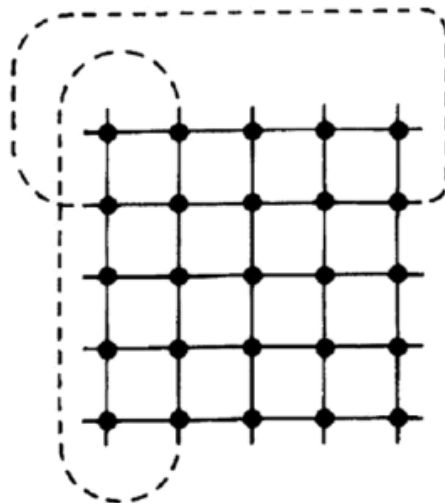


Figure 3.5: Typical periodic boundary conditions for the two-dimensional Ising model. Figure taken from 75.

### 3.2.4 Multi-Scale Approach with Density Functional Theory

$$E_{electrostatic} = \frac{q_1 q_2}{4\pi\epsilon_0\epsilon_r} e^2 \frac{1}{r} = q_1 q_2 I_{electrostatic} \quad (3.9)$$

Equation 3.9 can be used to calculate the electrostatic interaction between a pairs of ions, where  $q_1$  and  $q_2$  are the bare formal charges,  $r$  is the separation of the point charges and  $\epsilon_r$  is the bulk static relative dielectric constant. The interaction between all pairs of ions within the system are summed over when calculating the change in the energy of the system after performing a trial move in our Monte Carlo simulations. We separate out the parameter  $I_{electrostatic}$  in our simulations. The value is first calculated considering a purely classical, electrostatic case where only the bare formal charges on the ions are considered and the bulk dielectric constant of  $\text{Cu}_2\text{ZnSnS}_4$  is used. Using a value of 13.2 for  $\epsilon_r$  and 3.8 Å for  $r$ , which is the separation of nearest-neighbour Cu-Zn ions, gives a value of -0.284 eV for  $I_{electrostatic}$ . This treatment however only accounts for the Coulombic interaction between the point charges and neglects any changes in the electronic structure during defect formation. The screening effect of the electronic structure would be more significant for the microscopic dielectric constant than for the bulk, macroscopic dielectric constant. In this study therefore we scale the interaction energy,  $I_{interaction}$ , in the simulations by comparing the formation energy of a nearest-neighbour Cu-Zn anti-site defect pair calculated using the classical code GULP to that obtained using quantum mechanical hybrid-density functional theory and the VASP code, where effects of the electronic structure are included in the calculation. We found that the defect formation energy obtained using VASP was approximately 1.5 times that obtained with GULP, we therefore scaled the interaction energy by the same amount and so  $I_{DFT} = 1.5 \times I_{electrostatic} = -0.425$ . Through doing this we aim to scale the macroscopic dielectric constant to be closer to the value of the microscopic dielectric constant.

### 3.2.5 Quantification of Disorder Using Radial Distribution Functions

- Brief overview of what an RDF is

- See new lab book and make figures to explain
- Reproducing GS
- Cu-Zn RDF first peak to describe Cu Zn Cu layer
- Cu-Sn RDF first peak to describe Cu Sn Cu layer

### 3.2.6 Band Tailing from the Distribution of Electrostatic Potential

## 3.3 Calculation of Intrinsic Band Gap Broadening in $\text{Cu}_2\text{ZnSnS}_4$

## 3.4 Calculation of Optoelectronic Properties of Candidate Solar Absorber Materials

# Chapter 4

## Performance Bottlenecks in $\text{Cu}_2\text{ZnSnS}_4$

### 4.1 Thermodynamic Disordering of Cu & Zn Ions in $\text{Cu}_2\text{ZnSnS}_4$

#### 4.1.1 Spatial Extent of Disorder Amongst Cu and Zn Cations

- Recovery of kesterite ground state at T=50k? (Cu-Zn and Cu-Sn layers, see lab book pg 2): visuals of structure in VESTA and RDF of Cu-Zn and Cu-Sn pairs
- Visuals of configs from eris and RDFs across T range

#### 4.1.2 Band Tailing due to Fluctuations in Electrostatic Potential

R plots for distributions of electrostatic potential of Sn

### 4.2 Formation Energy of Sulfur Vacancies

We investigate the formation energy of charge neutral sulfur vacancies ( $V_S^0$ ) as a function of the sulfur chemical potential, which itself is a function of temperature and pressure. We therefore

can assess the formation energy of the vacancy under typical annealing conditions. Work from Scragg et al showed that annealing out Cu and Zn disorder can be a very time consuming process, therefore for most practical purposes some disorder will be ‘frozen in’ after annealing. Typical annealing conditions for  $\text{Cu}_2\text{ZnSnS}_4$  are at ?? K and it has been shown that lower pressures are more optimal for the sulfide (whereas higher pressures are better for the selenide) \*\*cite Adam?\*\*. This is due to the allotropes of S?

On-going calculations are being performed for the charged sulfur vacancies ( $\text{V}_S^{+1}$  and  $\text{V}_S^{+2}$ ) so that the minimum energy defect, accounting for all possible charge states, across the temperature and pressure range can be determined.

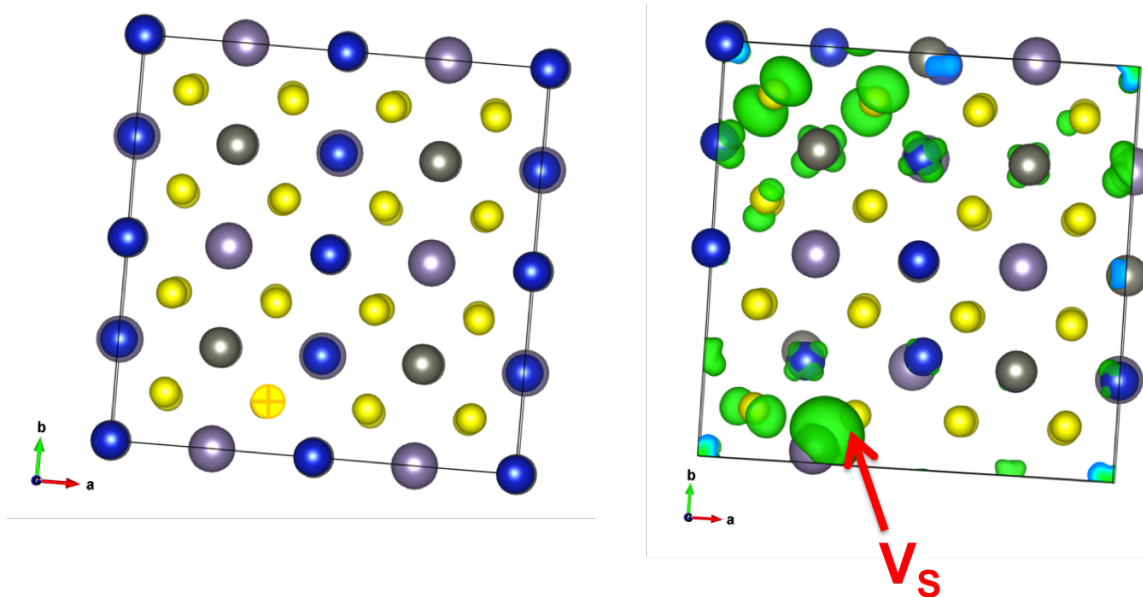


Figure 4.1: Perfect  $\text{Cu}_2\text{ZnSnS}_4$  supercell with S anion removed to form a sulfur vacancy ( $\text{V}_S$ ) indicated by a crosshair (left) and the calculated partial charge density of two excess electrons present for the charge neutral  $\text{V}_S$  (right).

## 4.3 Intrinsic Band Gap Broadening from Lattice Vibrations

# **Chapter 5**

## **Optoelectronic Properties of Sulfosalt Materials**

**5.1 Band Structures & Band Gaps**

**5.2 Dielectric Functions**

**5.3 Absorption Coefficients**

# **Chapter 6**

## **Conclusions**

### **6.1 Performance Bottlenecks of Cu<sub>2</sub>ZnSnS<sub>4</sub> Solar Cells**

### **6.2 Potential of Sulfosalt Materials for Solar Cell Devices**

### **6.3 Future Work**

- Simulations to determine most likely surface terminations to inform exptl strategies for surface passivation?
- QM/MM surface defect simulations?
- Further work on S vacancies?
- More properties of sulfosalt materials + calculations to predict FE?
- Further investigations with eris? Cu-poor CZTS?
- Extend eris Hamiltonian to next nearest neighbour interactions (likely to be important for long ranged coulomb interactions)

- Simulate larger systems with eris - domain formation and band gap fluctuations?

# Bibliography

- [1] T. Abzieher, T. Schnabel, M. Hetterich, M. Powalla, and E. Ahlswede. Source and effects of sodium in solution-processed kesterite solar cells. *Phys. Status Solidi*, 11:n/a–n/a, 2015.
- [2] N. Ashcroft and N. Mermin. *Crystal Lattices*. Saunders College Publishing, 1976.
- [3] N. Ashcroft and N. Mermin. *The Reciprocal Lattice*. Saunders College Publishing, 1976.
- [4] E. P. I. Association. Global market outlook for photovoltaics 2014-2018. 2014.
- [5] T. L. Bahers, M. Rérat, and P. Sautet. Semiconductors used in Photovoltaic and Photocatalytic Devices: Assessing Fundamental Properties from DFT. *J. Phys.* . . . , 2014.
- [6] M. Balkanski and R. F. Wallis. *Introduction to Transport in Semiconductors*. OUP Oxford, 2000.
- [7] W. Bao and M. Ichimura. Influence of Secondary Phases in Kesterite-Cu<sub>2</sub>ZnSnS<sub>4</sub> Absorber Material Based on the First Principles Calculation. *Int. J. Photoenergy*, 2014(c), 2014.
- [8] F. Bechstedt. *Many-Body Approach to Electronic Excitations*. Springer, 2015.
- [9] V. Belinicher and B. Sturman. The photogalvanic effect in media lacking a center of symmetry. *Uspekhi Fiz. Nauk*, 130(3):415, 1980.
- [10] A. Bhatnagar, A. Roy Chaudhuri, Y. Heon Kim, D. Hesse, and M. Alexe. Role of domain walls in the abnormal photovoltaic effect in BiFeO<sub>3</sub>. *Nat. Commun.*, 4(May):2835, 2013.

- [11] BISEM. *SMUD & BISEM-USA complete first ever PV Curtain Wall Retrofit project in USA*, 2010 (Accessed on May 17, 2016).
- [12] J. Blakemore. *Crystallinity and the Form of Solids: Reciprocal Space*. Cambridge University Press, 1985.
- [13] J. Blakemore. *Electrons in Metals: The band Theory of Solids*. Cambridge University Press, 1985.
- [14] K. W. Böer. *Handbook of the Physics of Thin-Film Solar Cells*. Springer, 2013.
- [15] M. Bokalič and M. Topič. *Spatially Resolved Characterization in Thin-Film Photovoltaics*.
- [16] R. L. Bonevitz. *Minerals*. Dorling Kindersley, Ltd, 2012.
- [17] S. Bourdais, C. Choné, B. Delatouche, A. Jacob, G. Laramona, C. Moisan, A. Lafond, F. Donatini, G. Rey, S. Siebentritt, A. Walsh, and G. Dennler. Is the Cu/Zn Disorder the Main Culprit for the Voltage Deficit in Kesterite Solar Cells? *Adv. Energy Mater.*, pages n/a–n/a, mar 2016.
- [18] R. E. Brandt, V. Stevanovi, D. S. Ginley, and T. Buonassisi. Identifying defect-tolerant semiconductors with high minority-carrier lifetimes: beyond hybrid lead halide perovskites. *MRS Communications*, 5:265–275, 6 2015.
- [19] F. Brivio, A. B. Walker, and A. Walsh. Structural and electronic properties of hybrid perovskites for high-efficiency thin-film photovoltaics from first-principles. *APL Mater.*, 1(4):042111, 2013.
- [20] P. Brody. Large polarization-dependent photovoltages in ceramic batio<sub>3</sub> + 5 wt.catio<sub>3</sub>. *Solid State Communications*, 12(7):673 – 676, 1973.
- [21] P. S. Brody. Semiconductor-ferroelectric nonvolatile memory using anomalous high photovoltages in ferroelectric ceramics. *Applied Physics Letters*, 38:153–155, Feb. 1981.
- [22] P. S. Brody and B. J. Rod. Decay of remanent polarization in ferroelectric films using polarization-dependent photovoltages. *Integrated Ferroelectrics*, 3(3):245–257, 1993.

- [23] K. T. Butler, J. M. Frost, and A. Walsh. Ferroelectric Materials for Solar Energy Conversion: Photoferroics Revisited. (December):1–11, 2014.
- [24] N. I. Butsko, I. D. Zhezhnich, and P. M. M. *Some Physical Properties of Stephanite in the Phase Transition Region*, 1973 (Accessed on September 3, 2015).
- [25] S. Chen, X. G. Gong, A. Walsh, and S.-H. Wei. Crystal and electronic band structure of cu<sub>2</sub>znsnx4 (x=s and se) photovoltaic absorbers: First-principles insights. *Applied Physics Letters*, 94(4):–, 2009.
- [26] S. Chen, X. G. Gong, A. Walsh, and S.-H. Wei. Defect physics of the kesterite thin-film solar cell absorber Cu<sub>2</sub>ZnSnS<sub>4</sub>. *Appl. Phys. Lett.*, 96(2):021902, 2010.
- [27] S. Chen, J.-H. Yang, X. G. Gong, A. Walsh, and S.-H. Wei. Intrinsic point defects and complexes in the quaternary kesterite semiconductor Cu<sub>2</sub>ZnSnS<sub>4</sub>. *Physical Review B*, 81(24):245204, June 2010.
- [28] W. S. Choi, M. F. Chisholm, D. J. Singh, T. Choi, G. E. Jellison, and H. N. t. . Lee.
- [29] A. G. Chynoweth. Surface space-charge layers in barium titanate. *Phys. Rev.*, 102:705–714, May 1956.
- [30] E. S. Cortezon, R. Aninat, and E. Sanchez-cortezon. Kesterite-based photovoltaic devices: Challenges for scale-up. In *Proceedings of the IEEE Photovoltaic Specialist*, 2016.
- [31] S. Curtarolo, G. L. W. Hart, M. B. Nardelli, N. Mingo, S. Sanvito, and O. Levy. The high-throughput highway to computational materials design. *Nat. Mater.*, 12(3):191–201, Mar. 2013.
- [32] J. P. Dakin and R. G. W. Brown. *Engineered Optical Materials*. CRC Press, 2010.
- [33] H. Dittrich, A. Bieniok, U. Brendel, M. Grodzicki, and D. Topa. Sulfosalts A new class of compound semiconductors for photovoltaic applications. *Thin Solid Films*, 515(15):5745–5750, May 2007.

- [34] H. Dittrich, A. Stadler, D. Topa, H. J. Schimper, and A. Basch. Progress in sulfosalt research. *Phys. Status Solidi Appl. Mater. Sci.*, 206(5):1034–1041, 2009.
- [35] Y. Dong, A. R. Khabibullin, K. Wei, J. R. Salvador, G. S. Nolas, and L. M. Woods. Bournonite pbcusbs3: Stereochemically active lone-pair electrons that induce low thermal conductivity. *ChemPhysChem*, pages n/a–n/a, 2015.
- [36] A. Eichler. *Sampling the Brillouin Zone*, 2014 (Accessed on April 28, 2015).
- [37] F. Espinosa-Faller. Neutron Diffraction and Xray Absorption Fine Structure Evidence for Local Lattice Distortions and Aperiodic Antisite Substitution in Cu<sub>2</sub>ZnSnS<sub>4</sub> Nanoparticles. *The Journal of Physical Chemistry C*, 118:26292–26303, 2014.
- [38] F. I. for Solar Energy Systems ISE. *Levelized Cost of Electricity Renewable Energy Technologies*, 2013 (Accessed on Aug 3, 2015).
- [39] V. Fridkin. *Photo-ferroelectrics*. Springer-Verlag Berlin Heidelberg, 1979.
- [40] J. M. Frost, K. T. Butler, F. Brivio, C. H. Hendon, M. van Schilfgaarde, and A. Walsh. Atomistic origins of high-performance in hybrid halide perovskite solar cells. *Nano Lett.*, 14(5):2584–90, May 2014.
- [41] V. Fthenakis. Sustainability of photovoltaics: The case for thin-film solar cells. *Renewable and Sustainable Energy Reviews*, 13(9):2746 – 2750, 2009.
- [42] T. Gershon, B. Shin, N. Bojarczuk, T. Gokmen, S. Lu, and S. Guha. Photoluminescence characterization of a high-efficiency Cu<sub>2</sub>ZnSnS<sub>4</sub> device. *J. Appl. Phys.*, 114(15):154905, 2013.
- [43] T. Gershon, B. Shin, T. Gokmen, S. Lu, N. Bojarczuk, and S. Guha. Relationship between Cu<sub>2</sub>ZnSnS<sub>4</sub> quasi donor-acceptor pair density and solar cell efficiency. *Appl. Phys. Lett.*, 103(May):2012–2015, 2013.
- [44] C. D. Ginley, David S. Cambridge University Press, 2012.

- [45] J. E. Girard. *Principles of Environmental Chemistry*. Jones & Bartlett Learning, LLC, 2014.
- [46] A. Goetzberger and V. U. Hoffmann. *Photovoltaic Solar Energy Generation*. Springer, 2005.
- [47] T. Gokmen, O. Gunawan, T. K. Todorov, and D. B. Mitzi. Band tailing and efficiency limitation in kesterite solar cells. *Applied Physics Letters*, 103(10):–, 2013.
- [48] T. Gokmen, O. Gunawan, T. K. Todorov, and D. B. Mitzi. Band tailing and efficiency limitation in kesterite solar cells. *Appl. Phys. Lett.*, 103(10):103506, 2013.
- [49] B. Goldstein and L. Pensak. *J. Appl. Phys.*, 155, 1959.
- [50] J. L. Gray. *The Physics of the Solar Cell*, pages 61–112. John Wiley & Sons, Ltd, 2005.
- [51] M. Grundmann. *The Physics of Semiconductors*. Springer, 2006.
- [52] D. P. Halliday, R. Claridge, M. C. Goodman, B. G. Mendis, K. Durose, and J. D. Major. Luminescence of  $Cu_2ZnSnS_4$  polycrystals described by the fluctuating potential model. *J. Appl. Phys.*, 113(22):2013, 2013.
- [53] W. Hermes, D. Waldmann, M. Agari, K. Schierle-Arndt, and P. Erk. Emerging Thin-Film Photovoltaic Technologies. *Chemie Ingenieur Technik*, 87(4):376–389, 2015.
- [54] J. Heyd, G. E. Scuseria, and M. Ernzerhof. Hybrid functionals based on a screened Coulomb potential. *J. Chem. Phys.*, 118(18):8207–8215, 2003.
- [55] K. Hönes, E. Zscherpel, J. Scragg, and S. Siebentritt. Shallow defects in  $Cu_2ZnSnS_4$ . *Phys. B Condens. Matter*, 404(23-24):4949–4952, 2009.
- [56] C. Honsberg and S. Bowden. *Open-Circuit Voltage*, 2014 (Accessed on April 28, 2015).
- [57] R. E. Hummel. *Electronic Properties of Materials*. Springer Science+Business Media, 2012.
- [58] M. Ichiki, H. Furue, T. Kobayashi, R. Maeda, Y. Morikawa, T. Nakada, and K. Nonaka. *Appl. Phys. Lett.*, 87:222903, 2005.

- [59] M. Ichiki, R. Maeda, Y. Morikawa, Y. Mabune, T. Nakada, and K. Nonaka. *Appl. Phys. Lett.*, 84:395–397, 2004.
- [60] M. Ichiki, Y. Morikawa, Y. Mabune, and T. Nakada. *J. Eur. Ceram. Soc.*, 24:1709–1714, 2004.
- [61] F. S. Inc. *Emissions from Photovoltaic Life Cycles*, 2009 (Accessed on April 18, 2015).
- [62] S. J. C. Irvine. RSC Energy and Environment Series, 2014.
- [63] K. Ito. *An Overview of CZTS-Based Thin-Film Solar Cells*. John Wiley & Sons, 2015.
- [64] K. Ito and T. Nakazawa. *Jpn. J. Appl. Phys.*, 27:2094–2097, 1998.
- [65] A. J. Jackson, D. Tiana, and A. Walsh. A universal chemical potential for sulfur vapours. *Chem. Sci.*, 00:1–11, 2015.
- [66] J. Jean, P. R. Brown, R. L. Jaffe, T. Buonassisi, and V. Bulovic. Pathways for Solar Photovoltaics. *Energy Environ. Sci.*, 2015.
- [67] W. Ji, K. Yao, and Y. C. Liang. *Adv. Mater.*, 22:1763–1766, 2010.
- [68] W. Ji, K. Yao, and Y. C. Liang. Bulk photovoltaic effect at visible wavelength in epitaxial ferroelectric bifeo<sub>3</sub> thin films. *Advanced Materials*, 22(15):1763–1766, 2010.
- [69] H. R. Johnson, R. H. Williams, and C. H. B. Mee. The anomalous photovoltaic effect in cadmium telluride. *Journal of Physics D: Applied Physics*, 8(13):1530, 1975.
- [70] A. K. Jonscher. *The Electronic Structure of Solids*. Routledge & Kegan Paul Ltd., 1965.
- [71] A. K. Jonscher. *The Imperfect Solid*. Routledge & Kegan Paul Ltd., 1965.
- [72] J. Kim, H. Hiroi, T. K. Todorov, O. Gunawan, M. Kuwahara, T. Gokmen, D. Nair, M. Hopstaken, B. Shin, Y. S. Lee, W. Wang, H. Sugimoto, and D. B. Mitzi. High efficiency cu<sub>2</sub>znsn(s,se)4 solar cells by applying a double in<sub>2</sub>s<sub>3</sub>/cds emitter. *Advanced Materials*, 26(44):7427–7431, 2014.

- [73] V. Kosyak, N. B. Mortazavi Amiri, A. V. Postnikov, and M. A. Scarpulla. Model of native point defect equilibrium in Cu<sub>2</sub>ZnSnS<sub>4</sub> and application to one-zone annealing. *J. Appl. Phys.*, 114(12), 2013.
- [74] P. Kral. Quantum kinetic theory of shift-current electron pumping in semiconductors. *Journal of Physics: Condensed Matter*, 12(22):4851, 2000.
- [75] D. P. Landau and K. Binder. *A Guide to Monte Carlo Simulations in Statistical Physics*. Cambridge University Press, 2015.
- [76] D. W. Lane, K. J. Hutchings, R. McCracken, and I. Forbes. *New Chalcogenide Materials for Thin Film Solar Cells*. The Royal Society of Chemistry, 2015.
- [77] M. Lang and A. Lang. *Overview Renewable Energy Sources Act*, 2014 (Accessed on 05 May, 2016).
- [78] J. P. Leitão, N. M. Santos, P. a. Fernandes, P. M. P. Salomé, a. F. da Cunha, J. C. González, G. M. Ribeiro, and F. M. Matinaga. Photoluminescence and electrical study of fluctuating potentials in Cu<sub>2</sub>ZnSnS<sub>4</sub> -based thin films. *Phys. Rev. B*, 84(2):024120, 2011.
- [79] R. Lesar. *The Monte Carlo Method*. Cambridge University Press, 2014.
- [80] S. Levchenko, V. E. Tezlevan, E. Arushanov, S. Schorr, and T. Unold. Free-to-bound recombination in near stoichiometric Cu<sub>2</sub>ZnSnS<sub>4</sub> single crystals. *Phys. Rev. B*, 86(4):045206, 2012.
- [81] M. E. Lines and A. M. Glass. Oxford University Press, 1977.
- [82] D. Ltd. *What is Levelised Cost of Energy (LCOE)?*, 2011 (Accessed on Aug 10, 2015).
- [83] S. Maske and B. J. Skinner. Studies of the sulfosalts of copper; i, phases and phase relations in the system cu-as-s. *Economic Geology*, 66:901–918, 1971.
- [84] A. McEvoy, T. Markvart, and L. C. ner. *Practical Handbook of Photovoltaics - Fundamentals and Applications*. Elsevier, 2012.

- [85] B. G. Mendis, M. D. Shannon, M. C. J. Goodman, J. D. Major, A. A. Taylor, D. P. Halliday, and K. Durose. The nature of electrostatic potential fluctuations in cu<sub>2</sub>znsns<sub>4</sub> and their role on photovoltaic device performance. *Journal of Physics: Conference Series*, 471(1):012014, 2013.
- [86] N. Metropolis, A. W. Rosenbluth, M. N. Rosenbluth, A. H. Teller, and E. Teller. Equation of State Calculations by Fast Computing Machines. *J. Chem. Phys.*, 21(6):1087–1092, 1953.
- [87] Y. Miyamoto, K. Tanaka, M. Oonuki, N. Moritake, and H. Uchiki. Optical Properties of Cu<sub>2</sub>ZnSnS<sub>4</sub> Thin Films Prepared by SolGel and Sulfurization Method. *Jpn. J. Appl. Phys.*, 47(1):596–597, 2008.
- [88] J. Nelson. *Generation and Recombination*. Imperial College Press, 2003.
- [89] J. Nelson. *Introduction*. Imperial College Press, 2003.
- [90] J. Neugebauer and T. Hickel. Density functional theory in materials science. *Wiley Interdiscip. Rev. Comput. Mol. Sci.*, 3(5):438–448, sep 2013.
- [91] M. E. J. Newman and G. T. Barkema. *The Ising Model and the Metropolis Algorithm*. Oxford University Press, 1999.
- [92] R. E. Newnham. *Dielectric Constant*. Oxford University Press, 2005.
- [93] U. D. of Energy. Energy efficiency and renewable energy: 2008 solar technologies market report. 2010.
- [94] U. of Oregon Investment Group. *First Solar, Inc*, 2011 (Accessed on 05 May, 2016).
- [95] M. I. of Technology. *The Future of Solar Energy*, 2015 (Accessed on June 9, 2015).
- [96] A. Orlova, R. Gainov, A. Dooglav, I. Penkov, and E. Korolev. Structure and transport properties of stephanite (ag<sub>5</sub>sbs<sub>4</sub>) according to antimony nuclear quadrupole resonance. *JETP Letters*, 96(6):370–374, 2012.

- [97] C. Paillard, X. Bai, I. C. Infante, M. Guennou, G. Geneste, M. Alexe, J. Kreisel, and B. Dkhil. Photovoltaics with Ferroelectrics: Current Status and Beyond. *Adv. Mater.*, apr 2016.
- [98] T. Pauporte and D. Lincot. ChemInform Abstract: Electrical, Optical and Photoelectrochemical Properties of Natural Enargite, Cu<sub>3</sub>AsS<sub>4</sub>. *Adv. Mater. Opt. Electron.*, 5:289–298, 1995.
- [99] G. Peng, X. Xu, and G. Xu. Hybrid organic-inorganic perovskites open a new era for low-cost, high efficiency solar cells. *Journal of Nanomaterials*, 2014.
- [100] C. Persson and A. Zunger. Anomalous grain boundary physics in polycrystalline cuinse<sub>2</sub>: The existence of a hole barrier. *Phys. Rev. Lett.*, 91:266401, Dec 2003.
- [101] C. Persson and A. Zunger. Compositionally induced valence-band offset at the grain boundary of polycrystalline chalcopyrites creates a hole barrier. *Appl. Phys. Lett.*, 87(21):211904, 2005.
- [102] J. Piprek. *Semiconductor Optoelectronic Devices: Introduction to Physics and Simulation*. Elsevier Science, 2003.
- [103] A. Polizzotti, I. L. Repins, R. Noufi, S.-H. Wei, and D. B. Mitzi. The state and future prospects of kesterite photovoltaics. *Energy Environ. Sci.*, 6:3171–3182, 2013.
- [104] A. Polman, M. Knight, E. C. Garnett, B. Ehrler, and W. C. Sinke. Photovoltaic materials: Present efficiencies and future challenges. *Science*, 352(6283), 2016.
- [105] P. Poosanaas, K. Tonooka, and K. Uchino. Photostrictive actuators. *Mechatronics*, 10(45):467 – 487, 2000.
- [106] I. E. A. P. P. S. Programme. Trends in photovoltaic applications, 19th edition. 2014.
- [107] M. Qin, Y. C. Yao, Kand Liang, and S. Shannigrahi. *J. Appl. Phys.*, 101:014104–014108, 2007.
- [108] K. Ramanathan and et al. *Prog. Photovolt. Res. Appl.*, 2003.

- [109] M. J. Romero, H. Du, G. Teeter, Y. Yan, and M. M. Al-Jassim. Comparative study of the luminescence and intrinsic point defects in the kesterite  $Cu_2ZnSnS_4$  and chalcopyrite  $Cu(In, Ga)Se_2$ . *Phys. Rev. B*, 84(16):165324, 2011.
- [110] T. Saga. Advances in crystalline silicon solar cell technology for industrial mass production. *NPG Asia Mater.*, 2(3):96–102, 2010.
- [111] H. W. Schock. *Adv. Solid State Phys.*, page 147, 1994.
- [112] S. Schorr. The crystal structure of kesterite type compounds: A neutron and x-ray diffraction study. *Solar Energy Materials and Solar Cells*, 95(6):1482 – 1488, 2011. Special Issue : Thin film and nanostructured solar cells.
- [113] S. Schorr, H.-J. Hoebler, and M. Tovar. A neutron diffraction study of the stannite-kesterite solid solution series. *Eur. J. Miner.*, 19(65):65–73, 2007.
- [114] I. Science and T. Directory. *List of Periodic Table Elements Sorted by Abundance in Earth's crust*, 1999 (Accessed on September 2, 2015).
- [115] J. J. S. Scragg, L. Choubrac, A. Lafond, T. Ericson, and C. Platzer-Björkman. A low-temperature order-disorder transition in Cu<sub>2</sub>ZnSnS<sub>4</sub> thin films. *Appl. Phys. Lett.*, 104(4):041911, Jan. 2014.
- [116] J.-S. Seol, S.-Y. Lee, J.-C. Lee, H.-D. Nam, and K.-H. Kim. Electrical and optical properties of cu<sub>2</sub>znsns<sub>4</sub> thin films prepared by rf magnetron sputtering process. *Solar Energy Materials and Solar Cells*, 75(12):155 – 162, 2003. {PVSEC} 12 Part {II}.
- [117] A. Shah, P. Torres, R. Tscharner, N. Wyrsch, and H. Keppner. Photovoltaic technology: The case for thin-film solar cells. *Science*, 285(5428):692–698, 1999.
- [118] Z. Shahan. *13 Charts On Solar Panel Cost & Growth Trends*, 2014 (Accessed on 15 May, 2016).
- [119] W. Shockley and H. J. Queisser. Detailed balance limit of efficiency of pn junction solar cells. *Journal of Applied Physics*, 32(3), 1961.

- [120] W. Shockley and W. T. Read. Statistics of the recombinations of holes and electrons. *Phys. Rev.*, 87:835–842, Sep 1952.
- [121] R. Shuey. *Semiconducting Ore Minerals*. Elsevier, 2012.
- [122] S. Siebentritt and S. Schorr. Kesterites-a challenging material for solar cells. *Prog. Photovoltaics Res. Appl.*, 20(February):512–519, 2012.
- [123] J. E. Sipe and A. I. Shkrebttii. Second-order optical response in semiconductors. *Phys. Rev. B*, 61:5337–5352, Feb 2000.
- [124] T. G. E. Society. *Introduction and the history of photovoltaics*. Routledge, 2013.
- [125] J. Starkiewicz, L. Sosnowski, and O. Simpson. *Nature*, 158, 1946.
- [126] S. Sun and P. A. Fuierer. Modeling of depolarization in ferroelectric thin films. *Integrated Ferroelectrics*, 23(1-4):45–64, 1999.
- [127] C. Tablero. The optical properties of CuPbSbS<sub>3</sub>-bournonite with photovoltaic applications. *Theor. Chem. Acc.*, 135(5):126, apr 2016.
- [128] S. Tajima, T. Itoh, H. Hazama, K. Ohishi, and R. Asahi. Improvement of the open-circuit voltage of cu 2 znsns 4 solar cells using a two-layer structure. *Applied Physics Express*, 8(8):082302, 2015.
- [129] R. J. D. Tilley. *Colour in Metals, Semiconductors and Insulators*. John Wiley & Sons, Ltd, 2011.
- [130] A. E. I. to the Knowledge of Mineralogy. *Capacitive Circuits*. Collins and Co., 1818.
- [131] P. R. Tulip. Dielectric and Lattice Dynamical Properties of Molecular Crystals via Density Functional Perturbation Theory: Implementation within a First Principles Code, 2004.
- [132] T. Unold, S. Kretzschmar, J. Just, O. Zander, B. Schubert, B. Marsen, and H.-W. Schock. Correlation between composition and photovoltaic properties of Cu<sub>2</sub>ZnSnS<sub>4</sub> thin film solar cells. *Photovolt. Spec. Conf. (PVSC)*, 2011 37th IEEE, pages 2820–2823, 2011.

- [133] T. Urban. *The Deal With Solar*, 2016 (Accessed on 23 April, 2016).
- [134] USGS. *Commodity Statistics and Information*, 2014 (Accessed on September 2, 2015).
- [135] M. D. Uspenskii, N. G. Ivanova, and M. I. E. *Sov. Phys.- Semicond*, page 1059, 1968.
- [136] P. Vela. SEM , EDX and EIS study of an electrochemically modified electrode surface of natural enargite ( Cu<sub>3</sub>AsS<sub>4</sub> ). 494:87–95, 2000.
- [137] J. Vidal. *UK and Germany break solar power records*, 2014 (Accessed on 04 May, 2016).
- [138] K. Wei, J. Martin, J. R. Salvador, and G. S. Nolas. Synthesis and characterization of bournonite pb<sub>2</sub>cu<sub>3</sub>bs<sub>3</sub> nanocrystals. *Crystal Growth & Design*, 15(8):3762–3766, 2015.
- [139] S.-Y. Wei, Y.-C. Liao, C.-H. Hsu, C.-H. Cai, W.-C. Huang, M.-C. Huang, and C.-H. Lai. Achieving high efficiency Cu<sub>2</sub>ZnSn(S,Se)<sub>4</sub> solar cells by non-toxic aqueous ink: Defect analysis and electrical modeling. *Nano Energy*, 26:74–82, aug 2016.
- [140] H. Wirth. *Recent Facts about Photovoltaics in Germany*, 2015 (Accessed on 04 May, 2016).
- [141] R. W. Wyckoff. *Am. J. Sci*, pages 349–359, 1928.
- [142] J. Yan and B. R. Saunders. Third-generation solar cells: a review and comparison of polymer:fullerene, hybrid polymer and perovskite solar cells. *RSC Adv.*, 4:43286–43314, 2014.
- [143] Y. Yan, W.-J. Yin, T. Shi, F. Hong, J. Ge, Y. Yue, W. Ke, D. Zhao, and A. Cimaroli. Theoretical and experimental study of earth-abundant solar cell materials. In *Active-Matrix Flatpanel Displays and Devices (AM-FPD), 2015 22nd International Workshop on*, pages 57–60, July 2015.
- [144] B. Yang, L. Wang, J. Han, Y. Zhou, H. Song, S. Chen, J. Zhong, L. Lv, D. Niu, and J. Tang. Cu<sub>2</sub>bs<sub>2</sub> as a promising earth-abundant photovoltaic absorber material: A combined theoretical and experimental study. *Chemistry of Materials*, 26(10):3135–3143, 2014.

- [145] S. Y. Yang, J. Seidel, S. J. Byrnes, P. Shafer, C. H. Yang, M. D. Rossell, P. Yu, Y. H. Chu, J. F. Scott, and J. W. Ager. *Nat. Nanotechnol.*, 5:143–147, 2010.
- [146] S. M. Young and A. M. Rappe. First principles calculation of the shift current photovoltaic effect in ferroelectrics. *Phys. Rev. Lett.*, 109(11):1–5, 2012.
- [147] S. M. Young, F. Zheng, and A. M. Rappe. First-principles calculation of the bulk photovoltaic effect in bismuth ferrite. *Phys. Rev. Lett.*, 109:236601, Dec 2012.
- [148] L. Yu, R. S. Kokenyesi, D. a. Keszler, and A. Zunger. Inverse design of high absorption thin-film photovoltaic materials. *Adv. Energy Mater.*, 3(1):43–48, 2013.
- [149] P. Y. Yu and M. Cardona. *Electronic Band Structures*. Springer-Verlag Berlin Heidelberg, 2010.
- [150] Y. Yuan, Z. Xiao, B. Yang, and J. Huang. Arising applications of ferroelectric materials in photovoltaic devices. *J. Mater. Chem. A*, 2(17):6027, 2014.
- [151] A. A. Zaky and R. Hawley. *Dielectric Solids*. Routledge & Kegan Paul, Ltd, 1970.
- [152] A. A. Zaky and R. Hawley. *Dielectrics in Static Fields*. Routledge & Kegan Paul, Ltd, 1970.
- [153] J. Zhang, X. Su, M. Shen, Z. Dai, L. Zhang, X. He, W. Cheng, M. Cao, and G. Zou. Enlarging photovoltaic effect: combination of classic photoelectric and ferroelectric photovoltaic effects. *Scientific Reports*, 3:2109, 2013.
- [154] H. Zhao and C. Persson. Optical properties of cu(in,ga)se<sub>2</sub> and cu<sub>2</sub>znsn(s,se)4. *Thin Solid Films*, 519(21):7508 – 7512, 2011. Proceedings of the {EMRS} 2010 Spring Meeting Symposium M: Thin Film Chalcogenide Photovoltaic Materials.